Combination of pembrolizumab and radiotherapy induces systemic antitumor immune responses in immunologically cold non-small cell lung cancer

Justin Huang[1,6], Willemijn S. M. E. Theelen[2,6], Zineb Belcaid[1,6], Mimi Najjar[1], Daphne van der Geest[2], Dipika Singh[1,3], Christopher Cherry[1], Archana Balan[1], James R. White[1], Jaime Wehr[1], Rachel Karchin[1,4], Noushin Niknafs[1], Michel M. van den Heuvel[5], Victor E. Velculescu[1], Kellie N. Smith[1,3], Paul Baas[2] & Valsamo Anagnostou[1,3] ✉

The abscopal effects of radiation may sensitize immunologically cold tumors to immune checkpoint inhibition. We investigated the immunostimulatory effects of radiotherapy leveraging multiomic analyses of serial tissue and blood biospecimens (n = 293) from a phase 2 clinical trial of stereotactic body radiation therapy (SBRT) followed by pembrolizumab in metastatic non-small cell lung cancer (NCT02492568). Participants with immunologically cold tumors (low tumor mutation burden, null programmed death ligand 1 expression or Wnt pathway mutations) had significantly longer progression-free survival in the SBRT arm. Induction of interferon-γ, interferon-α and antigen processing and presentation gene sets was significantly enriched after SBRT in nonirradiated tumor sites. Significant on-therapy expansions of new and pre-existing T cell clones in both the tumor (abscopal) and the blood (systemic) compartments were noted alongside clonal neoantigen-reactive autologous T cell responses in participants with long-term survival after radioimmunotherapy. These findings support the systemic immunomodulatory and antitumor effects of radioimmunotherapy and may open a therapeutic window of opportunity to overcome immunotherapy resistance.

Radiation therapy has the potential to enhance systemic immune responses in the context of immune checkpoint inhibition (ICI) through a variety of mechanisms[1–4]. Radiotherapy elicits immunogenic cell death that is an immunostimulatory program encompassing tumor-derived antigen processing and presentation, T cell priming, trafficking and migration and the induction of a permissive tumor microenvironment (TME)[1–4]. As such, the immunostimulatory effects of radiotherapy on priming and effector phases of antitumor immunity have been shown to mediate rejection of the irradiated tumor and nonirradiated metastatic sites, with the latter known as the abscopal effect[1]. The potential for therapeutic synergy between radiotherapy and ICI has been evidenced by numerous preclinical studies[1,5–7] and ICI after local tumor irradiation has been shown to induce the expansion of both intratumoral CD8+ T cells and potent abscopal responses[8]. Combined radioimmunotherapy can decrease regulatory CD4+ T cells while increasing effector memory, early activation and precursor-exhausted

CD8^{+} T cells[9]. While the immunomodulatory effects of radiotherapy have been described in the TME of irradiated tumors, much less is known about the biology of the abscopal effect that may be mediated by cytokine release and migration of activated effector T cells[10].

In tandem, despite the compelling rationale for combination radioimmunotherapy[11,12], the clinical efficacy of such approaches has not been consistently demonstrated, highlighting the unmet need to better understand the immunomodulatory effects of radiotherapy in the context of clinical trials and ultimately identify the subset of persons that may most benefit from these approaches. This is particularly timely for individuals with non-small cell lung cancer (NSCLC), where a sizable fraction develops primary or acquired resistance to ICI and where radioimmunotherapy has shown clinical efficacy in the metastatic[13,14], locally advanced[15] and resectable[16] settings. To address these questions, capture systemic antitumor immune responses and pinpoint the landscape of response to sequential radioimmunotherapy for individuals with metastatic NSCLC, especially in the context of immunologically cold tumors, we performed serial comprehensive multiomic analyses of nonirradiated tumors and their TME together with dynamic temporal investigation of the intratumoral and peripheral T cell repertoire, leveraging the randomized, phase 2 PEMBRO-RT trial of pembrolizumab after stereotactic body radiation therapy (SBRT) compared with pembrolizumab monotherapy (NCT02492568)[13]. We focused on putatively immunologically cold tumors (hereafter referred to as immunologically cold tumors), defined by a low tumor mutation burden (TMB < 300 mutations per exome), null programmed death ligand 1 (PDL1) expression or presence of mutations in the Wnt pathway, and linked our findings with mutation-associated neoantigen (MANA)-reactive T cell responses, ultimately suggesting that radioimmunotherapy may circumvent immunotherapy primary resistance of these tumors.

Results

Cohort and analysis overview

We examined serial nonirradiated tumor and peripheral blood samples collected from participants treated with pembrolizumab (200 mg kg^{-1} every 3 weeks) either alone (control arm) or in combination with SBRT (three doses of 8 Gy to a single tumor site before pembrolizumab initiation; SBRT arm) in the multicenter randomized phase 2 PEMBRO-RT clinical trial[13] (NCT02492568). We leveraged 293 serial peripheral blood and nonirradiated tumor samples collected at baseline and after 3–6 weeks of treatment (2 cycles of pembrolizumab) from 72 participants in the control (n = 37) and SBRT (n = 35) arms. Matched baseline and on-therapy nonirradiated tumor and blood samples were used for genomic, transcriptomic and T cell repertoire analyses (Methods and Supplementary Tables 1–4). In tandem, ex vivo autologous T cell cultures were pulsed with MANA-derived peptides to identify MANA-reactive T cell clones (Methods). Immunologically cold tumors defined as TMB-low (n = 43), PDL1-null (n = 41) or Wnt-mutated (n = 10) were separately studied (Methods).

Genomic features and PDL1 expression are differentially associated with response to radioimmunotherapy

We hypothesized that clinical responses with radioimmunotherapy would be encountered across the spectrum of TMB and PDL1 expression; to this end, we first assessed differential correlations between these biomarkers (indicative of immunologically hot tumors) and clinical outcomes in the SBRT and control groups. We computed TMB estimates from whole-exome sequencing (WES) (Methods and Supplementary Table 2) and, in line with previous studies[17], we found a correlation between TMB and radiographic response in participants in the control arm (Mann–Whitney U-test, P = 0.023). Consistent with our hypothesis, high TMB was not associated with therapeutic response in the SBRT arm (Mann–Whitney U-test, P = 0.53) (Fig. 1 and Supplementary Table 5). As reported in the PEMBRO-RT study[13], high PDL1 expression was associated

with radiographic response in the control arm (Mann–Whitney U-test, P = 0.00041), with a trend noted in the SBRT arm (Mann–Whitney U-test, P = 0.07) (Fig. 1 and Supplementary Table 5).

In evaluating differences in the mutational spectra and consistent with the TMB findings, we found an enrichment of the mutational smoking signature in responding tumors in the control arm (Mann–Whitney U-test, P = 0.019) but not the SBRT arm (Mann–Whitney U-test, P = 0.12) (Fig. 1 and Supplementary Table 5). Given the potential association between aneuploidy and response to combined radioimmunotherapy[18], we evaluated differences in aneuploidy among tumors with differential therapy responses (Methods, Fig. 1, Supplementary Tables 5 and 6, and Extended Data Fig. 1a,b). We did not detect a correlation between aneuploidy and clinical response in the SBRT arm (Supplementary Tables 5 and 6 and Extended Data Fig. 1b–d). In stratifying tumors in the SBRT arm by degree of aneuploidy, we noted that participants with highly aneuploid tumors had a numerically shorter progression-free survival (PFS) and overall survival (OS) (median PFS: 4.39 versus 15.56 months; log-rank test, P = 0.29; median OS: 9.89 versus 40.50 months; log-rank test, P = 0.13) (Extended Data Fig. 1c,d).

Next, we evaluated differential single-gene, pathway and comutation patterns, particularly focusing on capturing clinical responses with radioimmunotherapy in tumors harboring genomic features of resistance to ICI. We did not identify an enrichment in driver alterations by therapeutic response in either arm (Supplementary Table 7). Focusing on KRAS comutations, we did not identify an enrichment in KRAS;STK11, KRAS;KEAP1, KRAS;KEAP1;STK11 or KRAS;TP53 comutations in the SBRT arm. Similarly, in evaluating the differential enrichment of STK11 mutations by treatment arm, we did not detect an association between STK11 oncogenic mutations and therapy response (Fisher's exact test, P = 0.42) (Fig. 1) nor did we observe transcriptomic or T cell receptor (TCR) reshaping differences in these tumors (Extended Data Fig. 2a–d). Consistent with our previous studies[19], KRAS;TP53 comutations were enriched in responding tumors in the control arm (Fisher's exact test, P = 0.05) (Fig. 1 and Supplementary Table 7). Notably, we found a numerically higher frequency of mutations in genes in the canonical Wnt–β-catenin pathway in responding tumors in the SBRT arm, which was particularly interesting given the expected T cell exclusion of such tumors[20] (Fig. 1 and Supplementary Table 8). To orthogonally assess Wnt pathway status in tumors harboring Wnt mutations, we evaluated Wnt pathway signaling leveraging transcriptomic data and indeed found an upregulation in expression of Wnt signaling-associated gene sets in Wnt-mutated tumors (false discovery rate (FDR)-adjusted P = 0.046) (Supplementary Table 8). These findings indicated that clinical responses with radioimmunotherapy are encountered across the spectrum of immunologically cold and hot tumors, including tumors harboring features of immunotherapy resistance.

Serial transcriptomic analyses point to upregulation of adaptive immunity programs at nonirradiated metastatic sites after radioimmunotherapy

We next asked the question whether the synergistic therapeutic effect of ICI and SBRT, supported by the clinical outcomes in the PEMBRO-RT trial[13], was reflected in the induction of systemic inflammatory responses and remodeling of the TME of nonirradiated tumor sites. To this end, we assessed changes in the expression of immune-related pathways by RNA sequencing (RNA-seq) of serial nonirradiated tumor samples, collected at baseline and after two cycles of pembrolizumab ± SBRT (Methods and Supplementary Table 3). Gene set enrichment analysis (GSEA) was performed to evaluate differential expression of inflammatory and adaptive immunity programs (Methods). These analyses revealed significant post-SBRT and on-therapy upregulation of interferon-γ (IFNγ; normalized effect size (NES) = 2.60, FDR-adjusted P = 1.03 × 10^{-25}), IFNα (NES = 2.43, FDR-adjusted P = 1.64 × 10^{-12}), chemokine signaling (NES = 2.32, FDR-adjusted P = 2.78 × 10^{-14}), antigen processing and presentation (NES = 2.38, FDR-adjusted P = 2.28 × 10^{-10}), natural killer
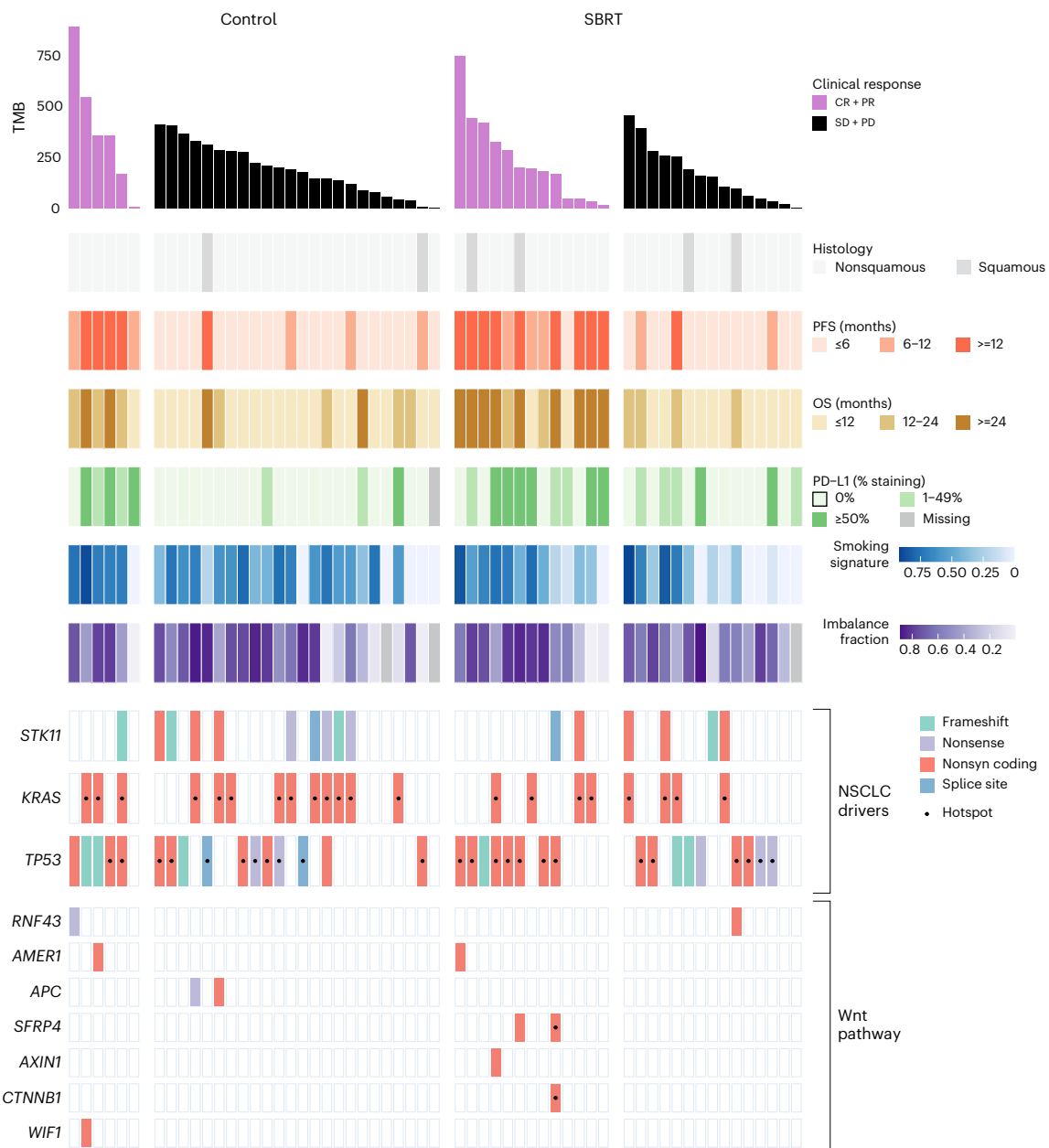
Fig. 1 | Genomic and molecular features of differential responses to immunotherapy and radioimmunotherapy. Participants are stratified by control versus SBRT arm and therapy response within each arm (CR + PR versus SD + PD); rows represent distinct features and columns represent individual participants. TMB correlated with radiographic response in the control arm (Mann–Whitney U-test, $P = 0.023$) but not the SBRT arm (Mann–Whitney U-test, $P = 0.53$). Similarly, PDL1 expression was associated with therapy response in the control arm (Mann–Whitney U-test, $P = 0.00041$), with a trend noted in the SBRT arm (Mann–Whitney U-test, $P = 0.07$). In line with the TMB findings, a mutational smoking signature was enriched in responding tumors in the control arm (Mann–Whitney U-test, $P = 0.019$) but not the SBRT arm (Mann–Whitney U-test, $P = 0.12$). Tumor aneuploidy (represented as the fraction of genome with allelic imbalance) was not correlated with response in the control or SBRT arms

(Mann–Whitney U-test, $P = 0.43$ and $P = 0.87$, respectively). Key NSCLC driver genes are shown together with annotations for hotspot mutations. We did not identify a differential enrichment in the overall number or in oncogenic mutations in *STK11*, *KRAS* or *TP53* by treatment arm; however, *KRAS;TP53* comutations were enriched in responding tumors in the control arm. A total of 16 tumors harbored *STK11* mutations, 13 of which are characterized as oncogenic in the literature (10 in the control arm and 3 in the SBRT arm). Of these 13 participants, there was 1 responding participant with an *STK11*-mutant tumor in the control arm and 1 responding participant with an *STK11*-mutant tumor in the SBRT arm (1/10, 10% versus 1/3, 33%; Fisher's exact test, $P = 0.42$). Notably, we observed an enrichment of Wnt pathway mutations in participants with tumors responding to SBRT (OS > 12 months; Fisher's exact test, $P = 0.047$).

(NK) cell cytotoxicity (NES = 2.50, FDR-adjusted $P = 9.13 \times 10^{-16}$), B cell receptor (BCR) signaling (NES = 2.48, FDR-adjusted $P = 5.66 \times 10^{-18}$) and other conserved inflammatory response gene sets in tumors in the SBRT arm (Fig. 2a and Supplementary Table 9). Each of these gene sets was more upregulated from baseline to on therapy in the SBRT arm than in the control arm (Fig. 2a and Supplementary Tables 9 and 10).

Notable on-therapy expression differences between the SBRT and control arms were also observed in the downregulation of gene sets related to cell-cycle progression (NES = −1.50, FDR-adjusted $P = 0.0188$), double-stranded DNA break repair (NES = −1.52, FDR-adjusted $P = 0.011$), Myc targets (NES = −2.16, FDR-adjusted $P = 6.63 \times 10^{-7}$), glycolysis (NES = −1.82, FDR-adjusted $P = 1.19 \times 10^{-5}$), ribosome biogenesis

(NES = −1.54, FDR-adjusted P = 0.021) and Sonic hedgehog signaling (NES = −1.68, FDR-adjusted P = 0.0072), all of which were more down-regulated in the SBRT arm compared with the control arm (Fig. 2b and Supplementary Tables 9 and 10). Overall, systemic radiation-induced effects spanned a number of immune gene expression programs (Methods, Fig. 2c–e and Supplementary Table 11) that were found to be upregulated with radioimmunotherapy in abscopal, nonirradiated tumor sites.

We next assessed dynamic changes in the abundance of immune cell subsets by deconvolution of serial transcriptomic data in the SBRT and control arms (Methods). In line with the GSEAs, several immune cell populations increased in absolute abundance on therapy within the SBRT cohort. We observed significant upregulation of CD8 T cells (Mann–Whitney U-test, P = 0.027) and M1 macrophages (Mann–Whitney U-test, P = 0.013) and a trend toward increased density of activated CD4 memory T cells (Mann–Whitney U-test, P = 0.074) and activated NK cells (Mann–Whitney U-test, P = 0.09) (Extended Data Fig. 3a–d and Supplementary Table 12). All deconvolution results are shown in Extended Data Fig. 3a–v. In contrast, these dynamic shifts were not apparent in on-therapy tumors in the control arm (Extended Data Fig. 3 and Supplementary Table 12). Taken together, these findings support that radioimmunotherapy may induce reshaping of the TME of abscopal tumor sites toward a more inflamed phenotype. Given the increased abundance in CD8 T cell population in on-therapy tumors with radioimmunotherapy, we next examined whether this coincided with an upregulation of coinhibitory receptors. We indeed found a significant upregulation of the inhibitory receptors PD1, LAG3 and TIM3 (FDR-adjusted P = 0.017, P = 0.026 and P = 0.009, respectively) with a similar trend observed for cytotoxic T lymphocyte antigen 4 (CTLA4) and TIGIT (FDR-adjusted P = 0.15 and P = 0.11, respectively) in on-therapy tumors in the SBRT arm (Supplementary Table 13). These findings are suggestive of the upregulation of coinhibitory receptors by tumor antigen stimulation in the context of radiation-induced immunogenic cell death and potentially open a therapeutic window of opportunity for further modulation of inhibitory pathways that can reverse T cell exhaustion and reinvigorate immune responses.

Interestingly, induction of BCR signaling was unique to the SBRT arm (Fig. 2a,c) (NES = 2.48, FDR-adjusted P = 5.66 × 10⁻¹⁸ in the SBRT arm and NES = 1.28, FDR-adjusted P = 0.15 in the control arm). To further investigate the effect of radioimmunotherapy on B cell responses, we performed bulk RNA-seq deconvolution and parsed BCR complementary-determining region 3 (CDR3) assemblies from baseline and on-therapy samples (Methods). BCR CDR3 count (reflecting BCR clonotypic density) was similar between responding and nonresponding tumors at baseline (Mann–Whitney U-test, P = 0.395) (Extended Data Fig. 4a and Supplementary Table 14) but significantly greater in responding tumors on therapy (Mann–Whitney U-test, P = 0.015) (Extended Data Fig. 4a and Supplementary Table 14). We next compared B cell density between on-therapy and baseline samples within each therapy arm, stratified by treatment response. Nonresponding tumors showed no difference in BCR CDR3 count between baseline and on-therapy samples in the control (Mann–Whitney U-test, P = 0.97) or SBRT arms (Mann–Whitney U-test, P = 0.74) (Supplementary Table 14). While our statistical power was limited by sample size, responding tumors in the SBRT arm showed a numerically greater BCR CDR3 count on therapy (Mann–Whitney U-test, P = 0.19) (Fig. 2f and Supplementary Table 14). As an example, we observed that three participants in the SBRT arm showed markedly greater BCR CDR3 counts on therapy than any participant in the control arm, which was reflective of durable clinical benefit on radioimmunotherapy for all three participants (Extended Data Fig. 4b and Supplementary Table 14). These findings provide anecdotal evidence for the potential of radioimmunotherapy to induce B cell expansions in the context of durable clinical benefit.

Transcriptomic analyses in long-term survivors undergoing radioimmunotherapy

Next, we sought to interpret the systemic effects of radioimmunotherapy on the basis of long-term outcomes, which would indirectly provide insights into the durability of the radiotherapy-induced systemic immune response. To this end, we performed differential expression gene set analyses of baseline and on-therapy tumors for participants with short-term versus long-term survival in the SBRT arm (Methods). At baseline, long-term survivors in the SBRT arm showed heightened expression of IFNγ (NES = 2.41, FDR-adjusted P = 6.69 × 10⁻¹⁶) and IFNα (NES = 2.32, FDR-adjusted P = 3.47 × 10⁻⁸) gene sets compared with SBRT short-term survivors (Supplementary Table 8). Notably, in the on-therapy samples from long-term survivors in the SBRT arm, we found an upregulation of a wider variety of immune-related pathways, including BCR signaling (NES = 2.54, FDR-adjusted P = 9.42 × 10⁻¹⁶), neutrophil degranulation (NES = 1.69, FDR-adjusted P = 5.18 × 10⁻⁶) and IFNγ (NES = 1.94, FDR-adjusted P = 5.28 × 10⁻⁶) gene sets (Fig. 2g and Supplementary Table 15). In tandem, baseline tumors of long-term

Fig. 2 | TME reshaping with radioimmunotherapy. a, Bar plot of the most upregulated gene sets in on-therapy tumors by treatment arm as ranked by adjusted P values from GSEA. A number of inflammatory gene sets were differentially upregulated in on-therapy tumors in the SBRT arm (n = 14 samples) compared with the control arm (n = 12 samples), including interactions between lymphoid and nonlymphoid cells (FDR-adjusted P = 7.35 × 10⁻³⁵ in the SBRT arm and P = 3.16 × 10⁻¹⁵ in the control arm), neutrophil degranulation (FDR-adjusted P = 1.46 × 10⁻³⁴ in the SBRT and P = 2.67 × 10⁻¹¹ in the control arm), IFNγ response (FDR-adjusted P = 1.03 × 10⁻²⁵ in the SBRT and P = 8.72 × 10⁻¹⁷ in the control arm) and overall inflammatory response (FDR-adjusted P = 5.31 × 10⁻¹⁷ in the SBRT arm and P = 4.58 × 10⁻⁹ in the control arm). A detailed description of all upregulated gene sets can be found in Supplementary Tables 9 and 10. **b**, Differentially downregulated gene sets in on-therapy tumors by treatment arm included cell-cycle targets of E2f transcription factors (FDR-adjusted P = 9.13 × 10⁻⁹ in the SBRT arm and P = 5.65 × 10⁻¹ in the control arm) and genes regulated by Myc (FDR-adjusted P = 6.63 × 10⁻⁷ in the SBRT arm and P = 9.78 × 10⁻¹ in the control arm). A detailed description of all downregulated gene sets can be found in Supplementary Tables 9 and 10. **c**, Heat map of GSEA results showing greater enrichment of immune programs from baseline to on therapy in the SBRT arm (n = 14 samples) compared with the control arm (n = 12 samples) across a broad range of immune gene sets. Each row represents a gene set; gene sets are grouped into ten categories shown in the legend. Enrichment scores were normalized by row to a maximum value of 1. **d**, Enrichment plot showing the leading edge of the IFNγ gene set, clearly upregulated on therapy in the SBRT arm (FDR-adjusted P = 1.03 × 10⁻²⁵). **e**, Enrichment plot showing the leading edge of the inflammatory response gene set, clearly upregulated on therapy in the SBRT arm (FDR-adjusted P = 5.31 × 10⁻¹⁷). **f**, Investigation of differences in B cell density in SBRT responders, who showed a numerically greater BCR CDR3 count on therapy than at baseline (mean: 3.24 × 10⁶ versus 2.45 × 10⁵; Mann–Whitney U-test, P = 0.19). **g**, Bar plot of the gene sets most enriched on therapy in SBRT long-term survivors (OS ≥ 3 years) versus SBRT short-term survivors (OS < 3 years), including interactions between lymphoid and nonlymphoid cells (FDR-adjusted P = 1.09 × 10⁻²⁹), BCR signaling (FDR-adjusted P = 9.42 × 10⁻¹⁶) and IFNγ response (FDR-adjusted P = 5.28 × 10⁻⁶). Extensive results can be found in Supplementary Table 15. **h**, Bar plot of the gene sets most downregulated on therapy in SBRT long-term survivors (OS ≥ 3 years) versus SBRT short-term survivors (OS < 3 years), including cell-cycle targets of E2f transcription factors (FDR-adjusted P = 3.64 × 10⁻¹⁴), G2/M checkpoint progression (FDR-adjusted P = 1.61 × 10⁻¹⁰), glycolysis (FDR-adjusted P = 1.20 × 10⁻⁸) and double-stranded DNA break repair (FDR-adjusted P = 1.95 × 10⁻⁵). Extensive results can be found in Supplementary Table 15. All statistical results are FDR-adjusted and two-sided P values. Box plots depict the median value and hinges correspond to the first and third quartiles. The whiskers extend from the corresponding hinge to the furthest value within 1.5× the interquartile range from the hinge. Dotted black horizontal lines indicate the FDR-adjusted P = 0.05. EMT, epithelial–mesenchymal transition; ID, immunodeficiency; Ag, antigen; iC, intracellular; RT, Reactome; HM, Hallmark; KG, Kegg.
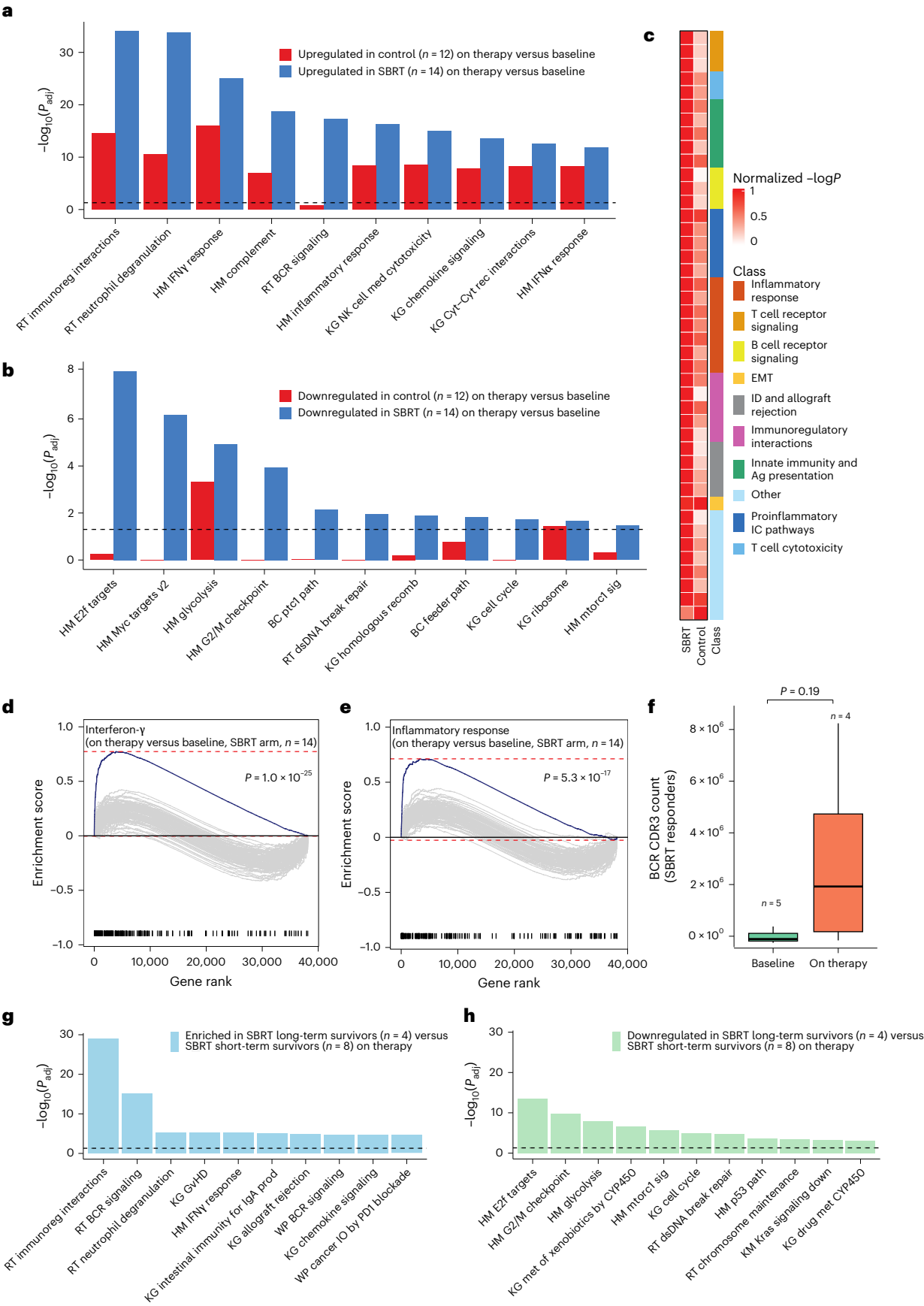
survivors in the SBRT arm showed significantly greater expression of cellular proliferation and cell-cycle progression gene sets (E2f targets: FDR-adjusted $P = 3.42 \times 10^{-21}$, NES = 2.59; G2/M checkpoint: FDR-adjusted $P = 1.68 \times 10^{-13}$, NES = 2.35) (Supplementary Table 8), which was reversed on therapy after radioimmunotherapy (E2f targets: FDR-adjusted $P = 3.64 \times 10^{-14}$, NES = −2.48; G2/M checkpoint: FDR-adjusted $P = 1.61 \times 10^{-10}$, NES = −2.31) (Fig. 2h and Supplementary Table 15). Furthermore, we found a downregulation in double-stranded DNA repair gene sets in on-therapy tumors of long-term responders (NES = −2.05, FDR-adjusted $P = 1.95 \times 10^{-5}$), which may reflect synergies between genomic instability and radiation-induced tumor immunogenicity. Taken together, these findings suggest that tumor immune infiltration and an inflamed TME at baseline is a favorable prognostic feature for long-term survival, which is further enhanced on therapy after radioimmunotherapy. Interestingly, while tumors of long-term survivors harbor transcriptional programs that point toward a high proliferation and DNA replication phenotype before therapy, these seem to be reversed after radioimmunotherapy; collectively, these findings suggest rewiring of cancer cells and their TME with radiotherapy.

Synergistic upregulation of adaptive immunity programs in TMB-low, PDL1-null or Wnt-mutated tumors with radioimmunotherapy

We subsequently evaluated whether the upregulation of inflammatory responses observed in the SBRT arm was also evident in immunologically cold tumors. Consistent with our findings in the whole cohort, in the TMB-low group, we observed significant post-SBRT and on-therapy upregulation of IFNγ (NES = 2.34, FDR-adjusted $P = 1.69 \times 10^{-12}$), IFNα (NES = 2.37, FDR-adjusted $P = 8.51 \times 10^{-9}$), chemokine signaling (NES = 2.24, FDR-adjusted $P = 7.94 \times 10^{-11}$), antigen processing and presentation (NES = 2.35, FDR-adjusted $P = 5.40 \times 10^{-8}$), NK cell cytotoxicity (NES = 2.16, FDR-adjusted $P = 1.43 \times 10^{-6}$) and conserved inflammatory response gene sets in tumors in the SBRT arm (Fig. 3a and Supplementary Table 16). The magnitude of on-therapy upregulation of each gene set was greater in the SBRT arm compared with the control arm (Supplementary Table 17). Similarly, in the PDL1-null group of the SBRT arm, we observed significant post-SBRT and on-therapy upregulation of IFNγ (NES = 2.89, FDR-adjusted $P = 3.94 \times 10^{-34}$), IFNα (NES = 2.71, FDR-adjusted $P = 1.29 \times 10^{-17}$), chemokine signaling (NES = 2.47, FDR-adjusted $P = 5.14 \times 10^{-15}$), antigen processing and presentation (NES = 2.60, FDR-adjusted $P = 1.15 \times 10^{-14}$), NK cell cytotoxicity (NES = 2.60, FDR-adjusted $P = 3.28 \times 10^{-16}$), BCR signaling (NES = 2.49, FDR-adjusted $P = 6.47 \times 10^{-15}$) and conserved inflammatory response

gene sets (Fig. 3b and Supplementary Table 18). Again here, the magnitude of on-therapy upregulation of each gene set was greater in the SBRT arm than the control arm (Supplementary Table 19). In the Wnt-mutated group, we found significant post-SBRT and on-therapy upregulation of similar inflammatory gene sets as noted in the PDL1-null and TMB-low groups. These included IFNγ (NES = 2.32, FDR-adjusted $P = 4.78 \times 10^{-13}$), IFNα (NES = 2.26, FDR-adjusted $P = 7.29 \times 10^{-9}$), antigen processing and presentation (NES = 2.35, FDR-adjusted $P = 6.49 \times 10^{-9}$) and BCR signaling (NES = 2.72, FDR-adjusted $P = 5.74 \times 10^{-26}$) (Supplementary Table 20). The greater enrichment of immune programs induced by SBRT extended to a broad range of inflammatory gene sets (Supplementary Table 11) in the TMB-low (Fig. 3c and Supplementary Table 16), PDL1-null (Fig. 3d and Supplementary Table 18) and Wnt-mutated (Fig. 3e and Supplementary Table 20) groups. As a representative example, IFNγ signaling was significantly upregulated on therapy in abscopal nonirradiated sites in each of the immunologically cold tumor subsets, indicating the mounting of systemic antitumor immune responses (Fig. 3f–h). Given the induction of tertiary lymphoid structures (TLSs) by immunogenic cell death, we postulated that TLSs may be upregulated at the nonirradiated tumor sites in the SBRT arm compared with the control arm. A TLS gene expression signature was indeed significantly upregulated on therapy in PDL1-null tumors in the SBRT arm (NES = 1.71, FDR-adjusted $P = 0.02$) (Extended Data Fig. 5a and Supplementary Table 8) but not in the control arm (NES = 1.22, FDR-adjusted $P = 0.45$) (Extended Data Fig. 5b and Supplementary Table 8). Furthermore, the TLS signature was significantly upregulated in Wnt-mutated tumors in the SBRT arm after SBRT and on therapy (NES = 1.90, FDR-adjusted $P = 0.002$) (Extended Data Fig. 5c and Supplementary Table 8). Collectively, these findings support the induction of systemic immune responses involving both T and B cell immunity and are suggestive of a potential 'cold-to-hot' conversion of the TME with radioimmunotherapy.

Radioimmunotherapy confers longer clinical outcomes in participants with immunologically cold tumors

Building on the differential association of TMB and PDL1 with therapy response in the SBRT arm compared with pembrolizumab monotherapy and prompted by the transcriptomic analyses supporting the abscopal effect of radioimmunotherapy, we sought to determine whether tumors that are less likely to respond to ICI monotherapy demonstrated radiographic responses with radioimmunotherapy (Fig. 4a). We first evaluated RECIST (response evaluation criteria in solid tumors) measurements of the biopsied nonirradiated lesions at baseline and

Fig. 3 | TME reshaping with radioimmunotherapy in immune cold tumors.
a, Bar plot of the 10 most upregulated gene sets from baseline to 3–6 weeks on therapy in TMB-low tumors in the SBRT ($n = 12$ samples) and control ($n = 11$ samples) arms, including neutrophil degranulation (FDR-adjusted $P = 4.93 \times 10^{-30}$ in the SBRT arm and $P = 1.58 \times 10^{-9}$ in the control arm), IFNγ response (FDR-adjusted $P = 1.69 \times 10^{-12}$ in the SBRT arm and $P = 5.97 \times 10^{-12}$ in the control arm), chemokine signaling (FDR-adjusted $P = 7.94 \times 10^{-11}$ in the SBRT arm and $P = 9.79 \times 10^{-6}$ in the control arm), overall inflammatory response (FDR-adjusted $P = 1.12 \times 10^{-9}$ in the SBRT arm and $P = 2.68 \times 10^{-7}$ in the control arm), and antigen processing and presentation (FDR-adjusted $P = 5.40 \times 10^{-8}$ in the SBRT arm and $P = 1.92 \times 10^{-5}$ in the control arm). Extensive findings can be found in Supplementary Table 16. **b**, Bar plot of the 10 most upregulated gene sets from baseline to 3–6 weeks on therapy in PDL1-null tumors in the SBRT ($n = 9$ samples) and control ($n = 9$ samples) arms, including IFNγ response (FDR-adjusted $P = 3.94 \times 10^{-34}$ in the SBRT arm and $P = 5.52 \times 10^{-6}$ in the control arm), IFNα response (FDR-adjusted $P = 1.29 \times 10^{-17}$ in the SBRT arm and $P = 1.08 \times 10^{-2}$ in the control arm), NK cell cytotoxicity (FDR-adjusted $P = 3.28 \times 10^{-16}$ in the SBRT arm and $P = 6.43 \times 10^{-6}$ in the control arm), BCR signaling (FDR-adjusted $P = 6.47 \times 10^{-15}$ in the SBRT arm and $P = 0.84$ in the control arm), and antigen processing and presentation (FDR-adjusted $P = 1.15 \times 10^{-14}$ in the SBRT arm and $P = 3.73 \times 10^{-5}$ in the control arm). Extensive findings can be found in Supplementary Table 16.

c–e, Heat map of GSEAs showing the most upregulated immune gene sets from baseline to 3–6 weeks on therapy in TMB-high tumors in the SBRT arm ($n = 4$ samples), TMB-low tumors in the SBRT arm ($n = 11$ samples) and TMB-low tumors in the control arm ($n = 10$ samples) (**c**), in PDL1-positive tumors in the SBRT arm ($n = 6$ samples), PDL1-null tumors in the SBRT arm ($n = 8$ samples), PDL1-positive tumors in the control arm ($n = 4$ samples) and PDL1-null tumors in the control arm ($n = 8$ samples) (**d**), and in Wnt wild-type tumors in the SBRT arm ($n = 12$ samples), Wnt-mutated tumors in the SBRT arm ($n = 2$ samples) and Wnt wild-type tumors in the control arm ($n = 10$ samples) (**e**). Each row represents a gene set; gene sets are grouped into nine categories shown in the legend. Enrichment scores were normalized by row to a maximum value of 1. For every cohort stratification (TMB-high versus TMB-low, PDL1-positive versus PDL1-null and Wnt-mutated versus Wnt wild-type tumors), we observed greater enrichment of immune gene sets in the SBRT arm than the control arm across a broad range of immune gene sets. **f**, Enrichment plot of the IFNγ gene set in on-therapy tumors with low TMB in the SBRT arm ($n = 12$ samples; FDR-adjusted $P = 1.69 \times 10^{-12}$). **g**, Enrichment plot of the IFNγ gene set in on-therapy PDL1-null tumors in the SBRT arm ($n = 9$ samples; FDR-adjusted $P = 3.94 \times 10^{-34}$). **h**, Enrichment plot of the IFNγ gene set in on-therapy Wnt-mutated tumors in the SBRT arm ($n = 5$ samples) from baseline to 3–6 weeks on therapy (FDR-adjusted $P = 4.78 \times 10^{-13}$). All statistical results are two-sided P values. Dotted black horizontal lines indicate FDR-adjusted $P = 0.05$.

at 12 weeks for each participant (Methods). Baseline tumor measurements were similar between participants in the SBRT and control groups and across all subsets analyzed (TMB-low, TMB-high, PDL1-null, PDL1-positive, Wnt-mutated and Wnt wild-type tumors). Overall, the abscopal (biopsied) tumor sites in the SBRT arm had a notable decrease in RECIST measurements between 0 and 12 weeks (mean: 45.52 mm to 30.44 mm; Mann–Whitney U-test, $P = 0.05$) (Fig. 4b and Supplementary Table 21), whereas rebiopsied tumor sites in the control arm did not

show a significant change in RECIST measurements (mean: 45.48 mm to 44.85 mm; Mann–Whitney U-test, $P = 0.64$) (Supplementary Table 21). Similarly, in TMB-low and PDL1-null participants, we observed a notable regression in RECIST measurements of the biopsied abscopal site at 12 weeks in the SBRT arm (TMB-low mean: 47.93 mm to 30.44 mm; PDL1-null mean: 50.78 mm to 32 mm) (Fig. 4c, Supplementary Table 21 and Extended Data Fig. 6a), with similar trends in the Wnt-mutant subgroup (Extended Data Fig. 6b). Interestingly, the SBRT-associated
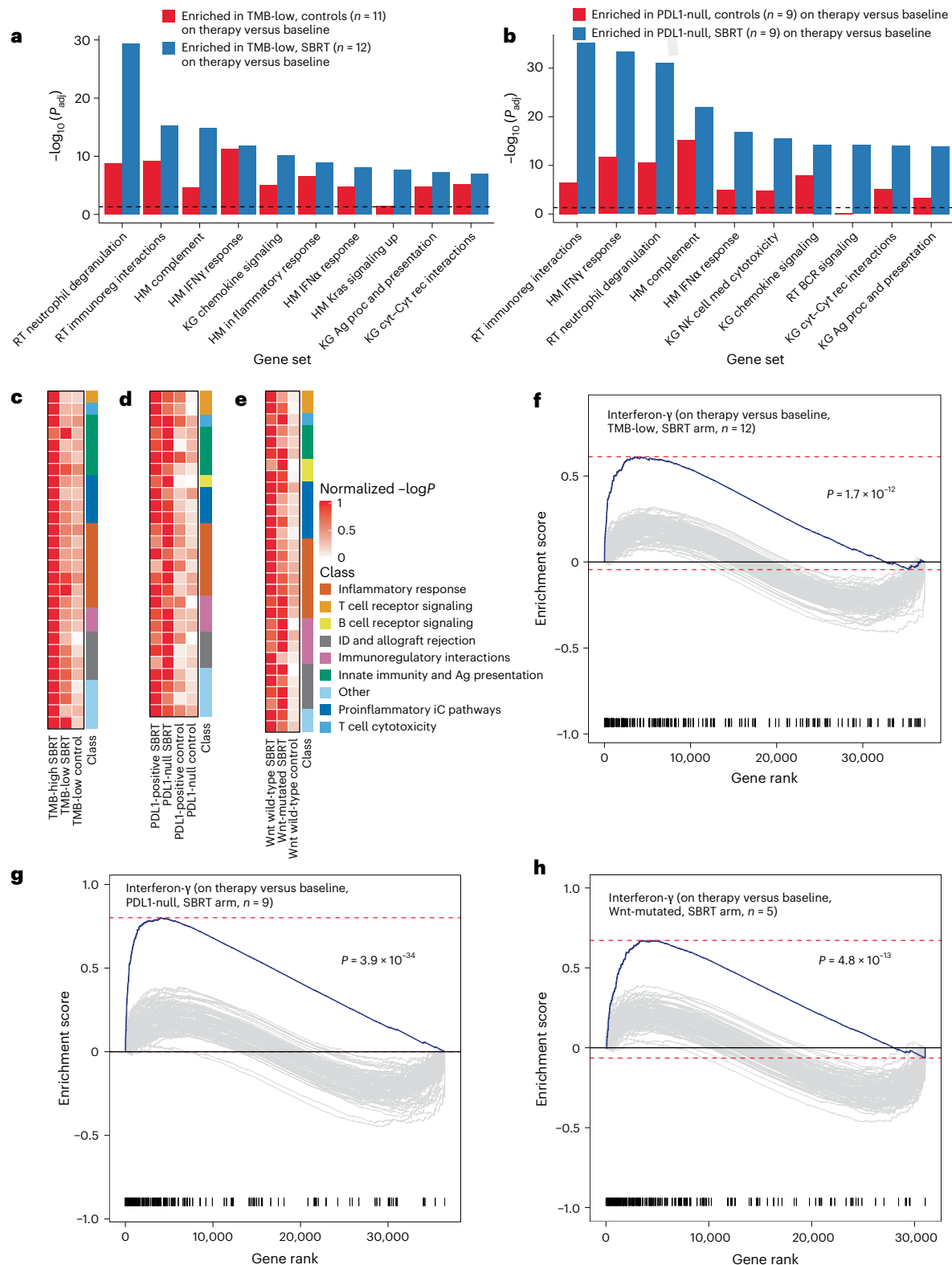
abscopal site tumor regression was not as pronounced in TMB-high and PDL1-positive tumors (Fig. 4c, Supplementary Table 21 and Extended Data Fig. 6a). These findings highlight the factual tumor regression of abscopal sites in the SBRT arm in comparison to the control arm associated with improved response.

In assessing survival outcomes, participants with tumors harboring TMB-low or PDL1-null expression attained significantly longer PFS in the SBRT arm (median PFS: 5.21 versus 1.81 months; log-rank test, $P = 0.029$) (Fig. 4d) compared with the control arm (median PFS: 4.22 versus 1.71 months; log-rank test, $P = 0.022$) (Fig. 4e). Similarly, participants in the SBRT arm with Wnt-mutated tumors ($n = 5$) had significantly longer PFS compared with those with wild-type tumors ($n = 30$) (median PFS: not reached versus 5.95 months; log-rank test, $P = 0.037$) (Fig. 4f). Notably, participants with TMB-high tumors ($n = 15$), PDL1-positive expression (≥1% staining on immunohistochemistry (IHC); $n = 29$), PDL1-high tumors (≥50% staining on IHC; $n = 15$) and PDL1-low tumors (1–49% staining on IHC; $n = 14$) did not attain longer PFS in the SBRT arm compared with the control arm (Extended Data Fig. 7a–d). Furthermore, there was no difference in PFS between participants with Wnt-mutated compared with wild-type tumors in the control arm (Extended Data Fig. 7e). Taken together, the survival analyses indicate that radioimmunotherapy may be particularly effective for tumors harboring features of ICI primary resistance. We then examined the difference in OS for these participants between treatment arms. Participants with tumors harboring Wnt mutations had a longer OS in the SBRT arm (median OS: not reached versus 9.92 months; log-rank test, $P = 0.013$) (Extended Data Fig. 8a). Similarly, participants with PDL1-null tumors showed a trend toward longer OS in the SBRT arm compared with the control arm (median OS: 7.21 versus 6.05 months; log-rank test, $P = 0.084$) (Extended Data Fig. 8b). Participants with TMB-low tumors attained a numerically longer OS in the SBRT arm compared with the control arm (median OS: 9.89 versus 6.70 months; log-rank test, $P = 0.16$) (Extended Data Fig. 8c).

To control for potential participant-related and technical factors that may confound the association between immunologically cold tumors and clinical response with radioimmunotherapy, we performed multivariate Cox regression analyses adjusting for age, gender, smoking status, tumor histology and tumor purity (Methods). Participants with low TMB tumors had a favorable hazard ratio (HR) for PFS in the SBRT arm (HR: 0.38, $P = 0.01$); similarly, participants with PDL1-null tumors had a favorable HR when receiving radioimmunotherapy (HR: 0.43, $P = 0.066$) (Supplementary Table 22). With respect to Wnt-mutated tumors, Wnt mutations were favorably associated with PFS (HR: 0.23, $P = 0.065$) and OS (HR: 0.19, $P = 0.046$) in the SBRT arm (Supplementary Table 22). Overall, these findings support the independent association between radioimmunotherapy and survival for participants with immunologically cold tumors.

## T cell repertoire reshaping and expansion of new T cell clones with radioimmunotherapy

Tying in the transcriptomic analyses, pointing toward mounting of systemic antitumor immune responses and a more permissive TME after radioimmunotherapy, with T cell repertoire dynamics and composition, we evaluated new and existing TCR clonotypic expansions in the nonirradiated tumor and peripheral blood compartments by TCR Vb CDR3 next-generation sequencing (Methods). To this end, we hypothesized that the noted upregulation of IFN signaling would result in an influx of T cells; as such, the abscopal effect of radiotherapy may be captured by detection of new and expanded TCR clones in the TME and blood compartments. Consistent with our hypothesis, we found a significantly higher density of new (Fig. 5a and Supplementary Table 23) and pre-existing (Fig. 5b and Supplementary Table 23) intratumoral TCR clones in abscopal tumor sites in the SBRT arm compared with the control arm (mean count of all clones: 34.83 versus 18.69, respectively; generalized linear model (GLM) Wald test, $P = 0.025$; mean count of new clones: 16.17 versus 7.54, respectively; Wald test, $P = 0.022$). Similar dynamics were observed in peripheral blood, supporting pre-existing and new clonotypic expansions in the SBRT arm compared with the control arm (mean count of all clones: 21.61 versus 8.15, respectively; Wald test, $P = 0.030$; mean count of new clones: 4.56 versus 1.00; Wald test, $P = 0.039$) (Fig. 5a,b and Supplementary Table 23). Focusing on TCR clones expanding in both nonirradiated tumor and blood compartments, we again found a higher density of TCR clonotypic expansions in the SBRT arm (Wald test, $P = 0.04$ for all clones and $P = 0.098$ for new clones) (Fig. 5a,b and Supplementary Table 16). TCR repertoire reshaping occurred independently of TMB and PDL1 expression, as both variables were incorporated into the GLM as covariates (Methods and Supplementary Table 23). Within the SBRT arm specifically, we did not observe significant differences in expanded clone counts between TMB-low and TMB-high tumors (intratumoral count of all clones: Mann–Whitney U-test, $P = 0.86$; intratumoral count of new clones: Mann–Whitney U-test, $P = 0.95$; blood count of all clones: Mann–Whitney U-test, $P = 0.43$; blood count of new clones: Mann–Whitney U-test, $P = 0.95$) (Fig. 5c and Supplementary Table 24) or between PDL1-null and PDL1-positive tumors (intratumoral count of all clones: Mann–Whitney U-test, $P = 0.33$; intratumoral count of new clones: Mann–Whitney U-test, $P = 0.17$; blood count of all clones: Mann–Whitney U-test, $P = 0.63$; blood count of new clones: Mann–Whitney U-test, $P = 0.075$) (Fig. 5d and Supplementary Table 25). These findings suggest that radioimmunotherapy induces expansion of both pre-existing and new T cell clones, an effect that was independent of TMB status and PDL1 expression. As a representative example of the immunomodulatory effects of radioimmunotherapy, participant CGLU727 who attained a partial response (PR) with radioimmunotherapy despite a TMB of 0.9 mutations per Mb and null PDL1

Fig. 4 | Differential outcomes and abscopal site tumor regression with radioimmunotherapy for participants with TMB-low, PDL1-null and Wnt-mutated tumors. a, Swimmer's plot showing OS and clinical and pathological features for each participant in the control (left) and SBRT (right) arms. Participants with TMB-low, PDL1-null or Wnt-mutated tumors were observed to attain the longest clinical outcomes in the SBRT arm. NA, not applicable. **b**, The abscopal (biopsied) tumor sites in the SBRT arm had a notable decrease in RECIST measurements between 0 and 12 weeks (mean: 45.52 mm to 30.44 mm; Mann–Whitney U-test, $P = 0.054$), whereas rebiopsied tumor sites showed no change in RECIST measurements in the control arm (Mann–Whitney U-test, $P = 0.64$). Extensive findings can be found in Supplementary Table 21. **c**, In TMB-low and PDL1-null participants, we observed a notable regression in RECIST measurements of the biopsied abscopal site in the SBRT arm (TMB-low mean: 47.93 mm to 30.44 mm, Mann–Whitney U-test, $P = 0.13$; PDL1-null mean: 50.78 mm to 32 mm; Mann–Whitney U-test, $P = 0.29$), which was not evident in the control arm. Interestingly, the SBRT-associated abscopal site tumor regression was not as pronounced in TMB-high and PDL1-positive tumors;

these had similar regressions in the SBRT and control arms. Extensive findings can be found in Supplementary Table 21. **d**, Kaplan–Meier curve of probability of PFS in TMB-low participants ($n = 43$ participants) treated in the control arm ($n = 21$ participants) and SBRT arm ($n = 22$ participants). TMB-low participants had longer PFS in the SBRT arm than in the control arm (median PFS: 5.21 versus 1.81 months; log-rank test, $P = 0.029$). **e**, Kaplan–Meier curve of probability of PFS in PDL1-null participants ($n = 41$ participants) treated in the control arm ($n = 23$ participants) and SBRT arm ($n = 18$ participants). PDL1-null participants had longer PFS in the SBRT arm than in the control arm (median PFS: 4.22 versus 1.71 months; log-rank test, $P = 0.022$). **f**, Kaplan–Meier curve of PFS in the SBRT arm ($n = 28$ participants) in the Wnt-mutated ($n = 5$ participants) and Wnt wild-type ($n = 23$ participants) groups. In the SBRT arm, participants with Wnt-mutated tumors had longer PFS compared with the wild-type subgroup (median PFS: not reached versus 5.45 months; log-rank test, $P = 0.02$). Box plots depict the median value and hinges correspond to the first and third quartiles. The whiskers extend from the corresponding hinge to the furthest value within 1.5× the interquartile range from the hinge.

expression, showed a pattern of TCR clonotypic expansion and reshaping in both TME (Fig. 5e, Supplementary Table 26 and Extended Data Fig. 9) and blood (Fig. 5f, Supplementary Table 26 and Extended Data Fig. 9) compartments. We subsequently evaluated the duration of TCR clonotypic expansions by serial sampling of blood and tumor tissue at the time of acquired resistance for a small number of participants for

which biospecimens were collected. While limited by sample size, we noted that only a small fraction of the intratumoral TCR clones that expanded at the time of response showed sustained expansion at the time of acquired resistance in two participants in the SBRT arm (7% sustained TCR expansions) and one participant in the control arm (3% sustained TCR expansions), with higher fractions detected in the
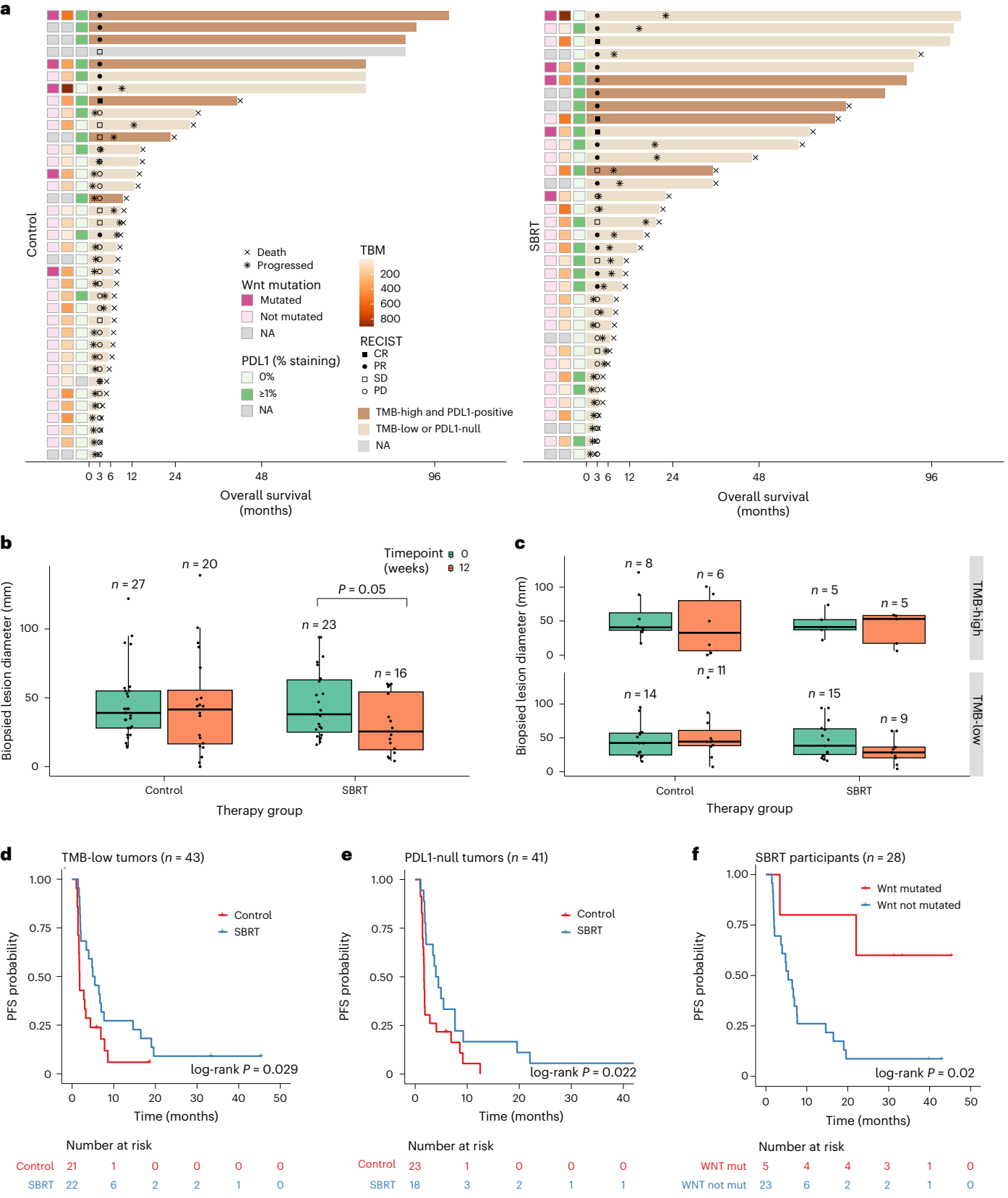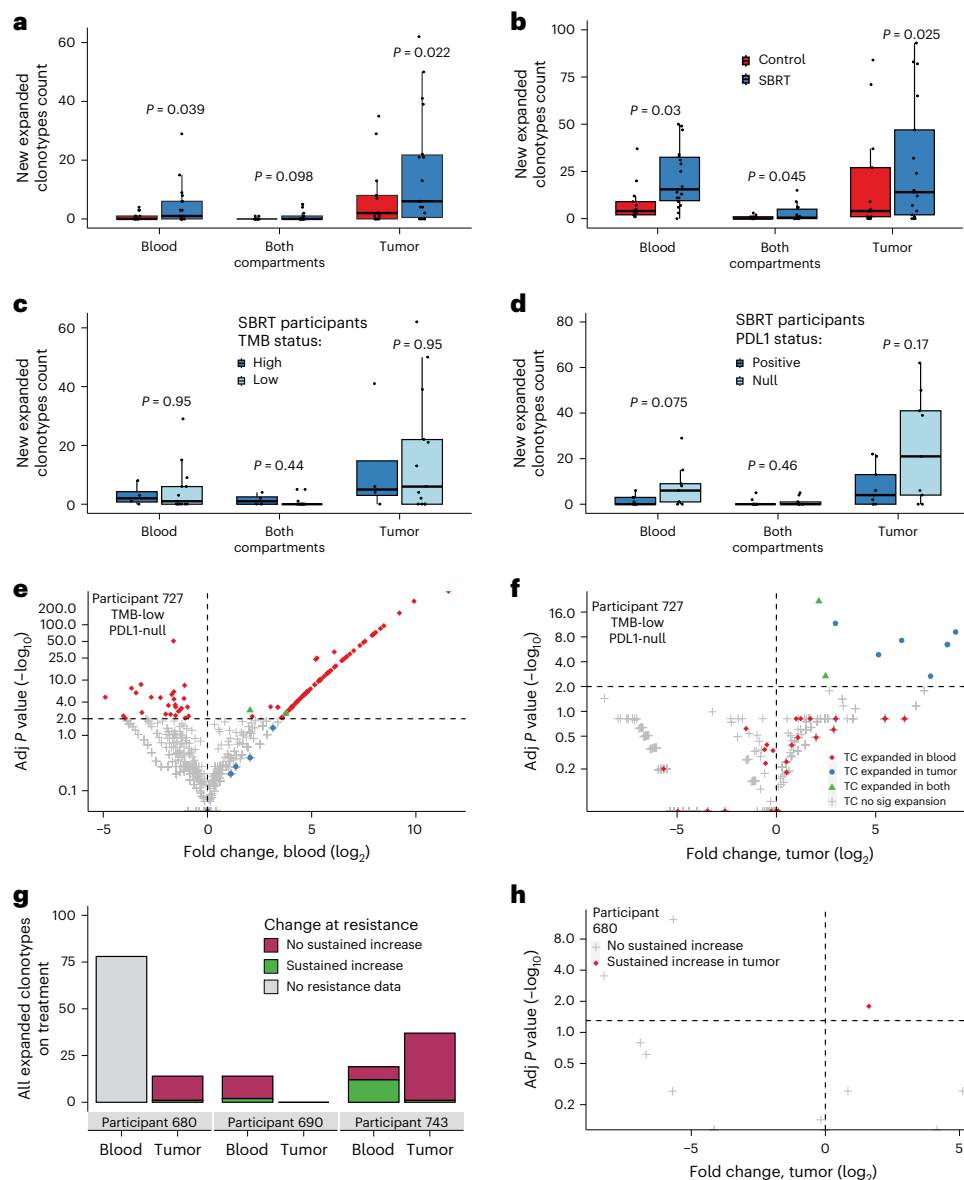
Fig. 5 | TCR clonotypic reshaping with radioimmunotherapy and longitudinal monitoring of the peripheral blood and intratumoral repertoire during therapy and at the time of acquired resistance. a, Counts of clonotypes expanded on therapy that were not observed at baseline in the blood and/or tumor compartments. There were significantly more newly expanded clones in blood alone and in tumor alone, with a trend of more newly expanded clones in both compartments (SBRT arm, $n = 18$ samples versus control arm, $n = 13$ samples; blood mean: 4.56 versus 1.00; Wald test (two-sided), $P = 0.039$; tumor mean: 16.17 versus 7.54; Wald test (two-sided), $P = 0.022$; both compartments mean: 1.00 versus 0; Wald test (two-sided), $P = 0.098$) in the SBRT cohort than control cohort. **b**, Counts of all clonotypes expanded on therapy relative to baseline in the blood and/or tumor compartments. There were significantly more expanded clones in all compartments in the SBRT cohort than control cohort (SBRT, $n = 18$ samples versus control arm, $n = 13$ samples; blood mean: 21.61 versus 8.15; Wald test (two-sided), $P = 0.030$; tumor mean: 34.83 versus 18.69; Wald test (two-sided), $P = 0.025$; both compartments mean: 2.61 versus 0.54; Wald test (two-sided), $P = 0.045$). **c**, Counts of new clonotypes expanded on therapy within the SBRT arm, stratified by TMB status. Counts of newly expanded clones were not significantly different between TMB-low ($n = 13$ samples) and TMB-high ($n = 4$ samples) tumors in the SBRT arm in either compartment (blood: Mann–Whitney U-test (two-sided), $P = 0.95$; tumor: Mann–Whitney U-test (two-sided), $P = 0.95$; both compartments: Mann–Whitney U-test (two-sided), $P = 0.44$). **d**, Counts of new clonotypes expanded on therapy within the SBRT arm, stratified by PDL1 status. Counts of newly expanded clones were not significantly

different between PDL1-null ($n = 9$ samples) and PDL1-positive ($n = 9$ samples) tumors in the SBRT arm in either compartment (blood: Mann–Whitney U-test (two-sided), $P = 0.075$; tumor: Mann–Whitney U-test (two-sided), $P = 0.17$; both compartments: Mann–Whitney U-test (two-sided), $P = 0.46$). **e,f**, TCR dynamics of newly expanded TCR clones in blood (**e**) and tumor (**f**) compartments for a participant with low TMB (0.9 mutations per Mb) and PDL1-null expression (0% on IHC) who exhibited PR in the SBRT cohort. Participant 727 had 14 total and 6 new clones expanded in the tumor and 34 total and 29 new clones expanded in the blood following SBRT and 2 cycles of pembrolizumab (Mann–Whitney U-test, two-sided). **g**, Clonotype dynamics at the time of resistance for clones that expanded on therapy in three PR tumors: two in the SBRT (participants 680 and 690) and one in the control arm (participant 743). Approximately 39% (12/31) of the clonotypes that expanded in blood and 4% (2/51) that expanded in the tumor on treatment across the 3 participants showed sustained increase at the time of resistance. At the participant level, most clones that expanded on treatment showed no sustained increase at the time of resistance (93% (13/14), 86% (12/14) and 77% (43/56) for the 3 participants). **h**, Expansion dynamics of all T cell clones that expanded in the tumor on treatment for participant 680 (PR in SBRT cohort; Mann–Whitney U-test, two-sided). Most clones did not show sustained increase at the resistance time point. Box plots depict the median value and hinges correspond to the first and third quartiles. The whiskers extend from the corresponding hinge to the furthest value within 1.5× the interquartile range from the hinge.
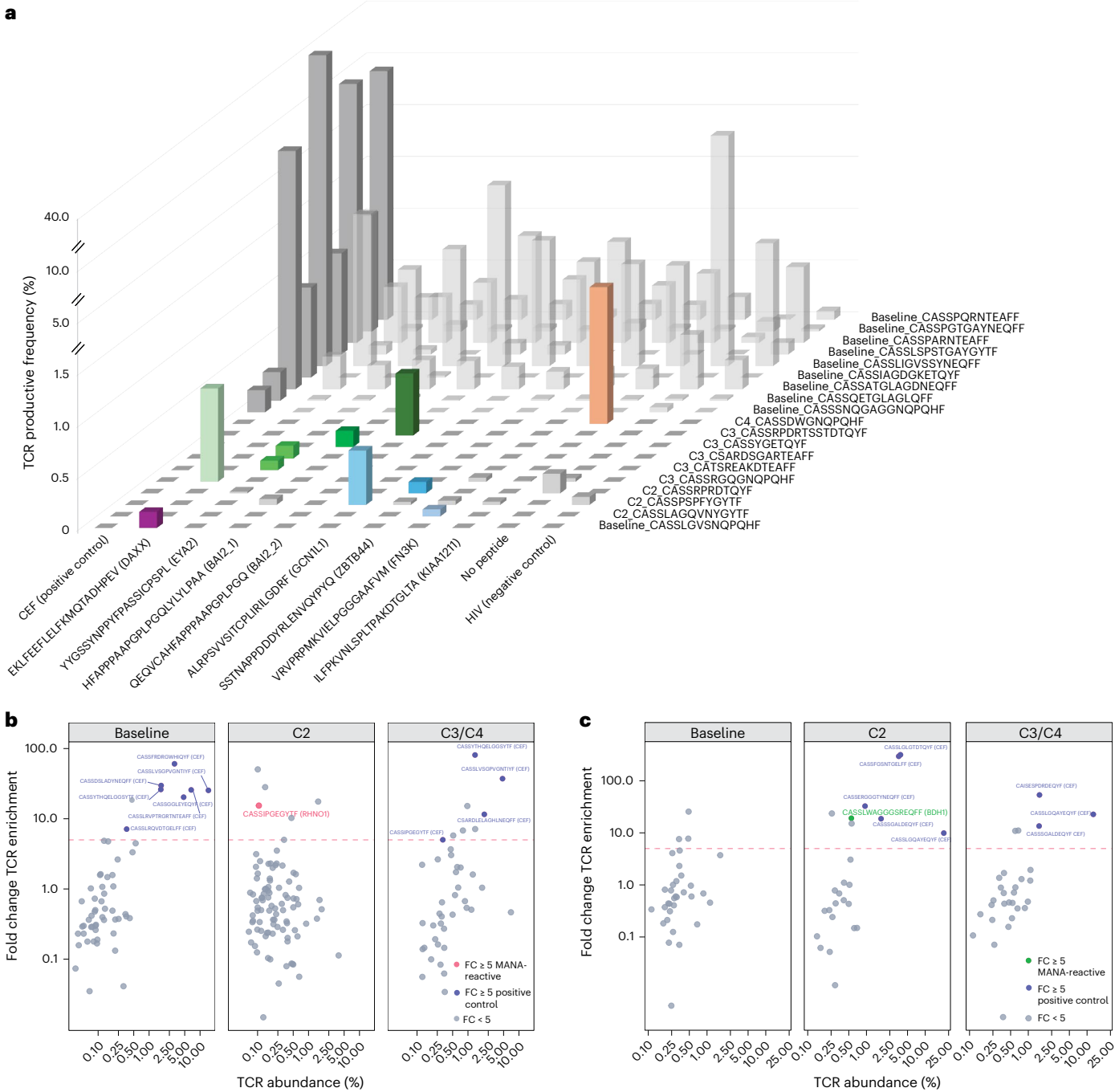
Fig. 6 | Neoantigen-reactive T cell responses in participants with long-term survival after radioimmunotherapy. We assessed neoantigen-specific T cell responses in three participants who attained radiographic response and long-term OS benefit in the SBRT arm. **a**, For participant CGLU680 who attained PR and an OS of 104 months, 10 neoantigen-reactive TCRs were detected specific to 8 MANAs across 4 time points (colored bars). Neopeptide sequences are listed on the horizontal axis with mutated genes in parentheses. TCR CDR3 amino acid sequences are listed along the depth axis with the time point of significant expansion prepended to each TCR sequence. Opaque dark-gray columns represent a significant expansion of T cell clones in response to the positive control peptide, while colored columns represent a significant expansion of T cell clones in response to cancer neopeptides. Opaque light-gray columns represent

a nonsignificant expansion of T cell clones in response to mutation-associated neopeptides. Translucent gray columns represent nonspecific clonotypic T cell expansions. **b**, For participant CGLU727 who attained PR and an OS of 46 months in the SBRT arm, the RHNO1 MANA-reactive TCR clone CASSIPGEGYTF was detected expanding at cycle 2. The TCR sequence is highlighted in red in the volcano plot, with the mutated gene in parentheses. **c**, For participant CGLU690 who attained PR with an OS of 102 months in the SBRT arm, the BDH1 MANA-reactive TCR clone CASSLWAGGGSREQFF was detected expanding at cycle 2. The TCR sequence is highlighted in green in the volcano plot, with the mutated gene in parentheses. C2, cycle 2 day 1; C3, cycle 3 day 1; C4, cycle 4 day 1; C3/C4, pooled PBMCs from cycle 3 day 1 and cycle 4 day 1.

blood compartment (14% in the SBRT and 63% in the control arm) (Fig. 5g,h, Supplementary Table 27 and Extended Data Fig. 10). Taken together, our findings suggest that combined radioimmunotherapy

may induce reshaping of the peripheral T cell repertoire together with abscopal responses in nonirradiated tumor sites that may drive tumor elimination and clinical responses.

Radioimmunotherapy induces systemic neoantigen-reactive T cell responses

We next hypothesized that the systemic effect of radiotherapy would be reflected in the detection of neoantigen-reactive T cell responses, targeting clonal expressed mutations that would be shared across the primary, irradiated and abscopal (biopsied) tumor sites. To test this hypothesis, we used the MANA functional expansion of specific T cells (MANAFEST) assay[21] to identify MANA-specific T cell clones (Methods) in 3 long-term survivors who attained PR in the SBRT arm despite their tumors harboring features of immunotherapy resistance (participant 680 with an OS of 104 months, participant 690 with an OS of 102 months and participant 727 with an OS of 46 months). We synthesized neopeptides using each tumor's WES data, followed by peptide stimulation of autologous T cells from each participant and identification of neoantigen-specific clonotypic amplifications by TCR sequencing (Methods and Supplementary Table 28). For participant CGLU680, we identified ten neoantigen-reactive TCR clones against clonal expressed mutations in *DAXX*, *FN3K*, *GCN1L1*, *ZBTB44*, *EYA2* and *KIAA1211* and a frameshift mutation in *BAI2*. Of note, the DAXX neopeptide-reactive clone was detected expanding in T cell cultures from baseline and cycle 3 on radioimmunotherapy, whereas the remainder of neoantigen-reactive clonotypic expansions were detected upon testing autologous T cell cultures procured after initiation of radioimmunotherapy (at cycles 2, 3 and 4 of pembrolizumab) (Fig. 6a and Supplementary Table 29). Furthermore, a *BDH1* mutation-associated neopeptide stimulated expansion of TCR clone CASSLWAGGGSREQFF in participant CGLU690 and, similarly, a *RHNO1* mutation-associated neopeptide stimulated expansion of TCR clone CASSIPGEGYTF in participant GGLU727, both after sequential radioimmunotherapy (Fig. 6b,c and Supplementary Tables 30 and 31). These findings support MANA-reactive T cell responses in long-term survivors receiving sequential radiotherapy and anti-PD1 therapy and provide further evidence to support the induction of systemic antitumor immune responses with radioimmunotherapy.

Discussion

Although preclinical studies support the synergistic role of radiotherapy and immunotherapy at both irradiated and nonirradiated sites[8,22–25], clinical trials for patients with advanced NSCLC have yielded mixed results. These shortcomings are amplified by the scarcity of studies supporting the systemic effects of radioimmunotherapy and induction of antitumor immune responses at nonirradiated tumor sites in the context of clinical trials[26]. To broaden our understanding of the systemic effects of radioimmunotherapy, we performed serial multiomic analyses of abscopal tumor sites together with their evolving TME and tied these findings to radiotherapy-induced peripheral and intratumoral T cell repertoire reshaping and MANA-reactive T cell responses in the PEMBRO-RT clinical trial of radioimmunotherapy (NCT02492568). These analyses revealed an induction of systemic immune responses with radioimmunotherapy including tumors harboring molecular features of immunotherapy resistance, likely driven by MANA cross-presentation in abscopal tumor sites. Our findings support the immunomodulatory effects of radiation together with a path forward for radioimmunotherapy as a potential strategy to overcome immunotherapy resistance.

Radiotherapy has been shown to drive immunogenic cell death through means such as induction of the cyclic GMP–AMP synthase (cGAS)–stimulator of IFN genes (STING) and type I IFN pathways[10,27,28], induced upregulation of major histocompatibility complex (MHC) molecules[29] and presentation of neoantigens at the irradiated site. While radiotherapy has also been shown to have immunosuppressive effects at the irradiated tumor site[18] through induction of PDL1 expression on tumor cells[30], addition of pembrolizumab, an anti-PD1 antibody, may be synergistic by counteracting this negative effect on the antitumor immune response and help explain why abscopal effects by radiotherapy alone are rare in the clinical setting. The premise of radiotherapy outside of local effects and disease control lies in the ability to elicit adaptive cytotoxic T cell responses recruited to nonirradiated sites[2,31,32]. Following radiotherapy, dendritic cells at the irradiated sites may capture tumor antigens and then cross-present these antigens in draining lymph nodes to prime new T cell responses[33]. In line with this notion[11,34], the pronounced reshaping of the TCR repertoire, including expansions of new TCR clones, at nonirradiated sites observed in the SBRT cohort suggested a radiation-driven abscopal effect in our cohort. The presence of a radioimmunotherapy-induced systemic antitumor immune response was further supported by the identification of neoantigen-reactive T cell clones in autologous T cells from participants attaining radiographic response and long-term survival in the SBRT arm. While the yield of functional T cell assays may be limited after radiotherapy given the known radiosensitivity of circulating lymphocytes and T cells[10], which may in turn be reflected in the smaller fraction of neoantigen-reactive T cell expansions detected at nonbaseline time points, our findings support MANA-reactive T cell responses in long-term survivors after radioimmunotherapy. In tandem, a broad array of inflammatory response gene expression programs were upregulated in nonirradiated tumor sites in our study, supporting the role of radioimmunotherapy in enriching systemic immune responses at nonirradiated sites beyond direct T cell cytotoxicity. Notably, induction of B cell responses on therapy was unique to the SBRT arm, with marked B cell expansion observed in a few SBRT participants who sustained durable clinical responses, highlighting the potential role of humoral adaptive responses in driving tumor regression after radioimmunotherapy. These findings align with our previous studies, supporting the role of SBRT in inducing systemic neoantigen-specific T cell responses in persons with early-stage NSCLC receiving definitive radiotherapy[35].

Immunologically cold NSCLC tumors, characterized by low TMB or low PDL1 expression, are typically less likely to regress with ICI when administered as monotherapy[36]. We found that the systemic immune-stimulatory benefits of radioimmunotherapy coincided with significantly improved therapeutic response and longer survival in this subset of persons when compared with pembrolizumab alone. In contrast, such associations were not noted for participants with immunologically hot tumors characterized by high TMB or high PDL1 expression, suggesting that the addition of SBRT to pembrolizumab may have limited benefit for this subpopulation. Similarly, activation of the Wnt–β-catenin pathway has also been linked with tumor immune evasion[20] and immunotherapy resistance[37]. Immunotherapy resistance may be driven by a causal relationship between tumor cell-intrinsic oncogenic activation of β-catenin and T cell exclusion, resulting in impaired host priming of antigen-specific T cells and impaired trafficking of effector T cells into the TME[38]. Interestingly, we detected an improved PFS for participants with Wnt-mutated tumors compared with wild-type tumors in the radioimmunotherapy arm. As a representative example, a tumor harboring an oncogenic *CTNNB1* gain-of-function hotspot mutation and a hotspot missense likely Wnt-activating mutation in *SFRP4* attained a complete response (CR) with radioimmunotherapy. The improved clinical response to radioimmunotherapy in participants with Wnt-mutated tumors may stem from the induction of cytotoxic T cell responses with radiation, partially overcoming the impaired priming and trafficking of T cell responses characteristic of these tumors.

While the statistical power of certain subset analyses was limited by the small sample size, potentially leading to type II error, our findings suggest that radioimmunotherapy may be effective in immunologically cold tumors that harbor features of primary resistance and may explain why clinical trials of unselected participants with solid tumors including advanced NSCLC have often yielded mixed results[22,23,39–42]. To this end, our findings may inform participant selection for radioimmunotherapy approaches including the subset of persons with primary resistance to immunotherapy that currently lacks effective treatment

options. Certainly, given the multifaceted nature of immunologically cold tumors that are driven by the interplay between tumor genotypes and TME phenotypes, future studies are needed to validate the role of radioimmunotherapy in tumors with overlapping characteristics of immunotherapy resistance.

Tumor aneuploidy has previously been shown to correlate with immunotherapy resistance in persons with metastatic NSCLC treated with sequential radioimmunotherapy[18]. In our study, we found a numerically shorter yet not statistically significant PFS and OS for participants with highly aneuploid tumors in the SBRT arm. We believe that this difference may be in part attributed to the types of tumor samples analyzed, as our study focuses on nonirradiated and abscopal lesions rather than irradiated lesions. Furthermore, our study design did not allow for evaluation of the immunomodulatory effect of concurrent radioimmunotherapy driven by cGAS–STING signaling in the context of radiation-induced DNA damage and concurrent anti-CTLA4 therapy[43], which may be heightened in tumors harboring a high degree of genomic instability[18]. As such, the role of tumor aneuploidy in therapy response may be context dependent and our findings highlight the complexity of identifying the subset of tumors and hosts that maximally benefit from radioimmunotherapy approaches.

Despite the findings of our study, the clinical translation of the immunomodulatory effects of radiotherapy has not been straightforward. Participant selection for radioimmunotherapy approaches remains key together with SBRT dose and timing. The underlying premise of radiotherapy lies first in its potential to sensitize immunologically cold tumors to ICI and overcome primary resistance in these populations and second in reinvigorating antitumor immune responses after progression on anti-PD(L)1 therapy. The latter is currently being tested in the RAD-IO clinical trial (NCT05401786), which incorporates rechallenging with anti-PD1 therapy after immune priming by ipilimumab and immune boosting by radiotherapy for participants with advanced NSCLC; in this trial, multiple metastatic sites are irradiated to counteract tumor heterogeneity and divergent antitumor immune responses. Additional clinical trials are needed to specifically investigate the benefit of radioimmunotherapy over immunochemotherapy or in overcoming immunotherapy resistance in persons with immunologically cold tumors. In conclusion, our study supports the abscopal effect of radioimmunotherapy in persons with metastatic NSCLC, including persons with immunologically cold tumors. Our findings suggest that radioimmunotherapy may be a promising avenue of further exploration for persons with therapeutic resistance to ICI; future efforts will specifically investigate the benefit of radioimmunotherapy in selected populations.

Methods

Cohort description and clinical response assessments
The study protocol was approved by the Institutional Review Board of Johns Hopkins University (Johns Hopkins Medicine Institutional Review Board) and the Netherlands Cancer Institute Antoni van Leeuwenhoek Institutional Review Board (registered under number CFMPB573). Written informed consent was provided by all study participants; participants were not compensated. We examined serial tumor and peripheral blood samples collected from participants treated with pembrolizumab (200 mg kg⁻¹ every 3 weeks) either alone (control arm) or in combination with SBRT (three doses of 8 Gy to a single tumor lesion; SBRT arm) during the multicenter randomized phase 2 PEMBRO-RT clinical trial (NCT02492568)[13]. This trial enrolled 92 participants with advanced NSCLC between July 1, 2015 and March 31, 2018, regardless of PDL1 status. Of those 92 participants, 76 were randomized to the control arm ($n = 40$) or the SBRT arm ($n = 36$) and biospecimens were procured for all participants who received at least one dose of pembrolizumab ($n = 72$ total: $n = 37$ in the control arm and $n = 35$ in the SBRT arm). Treatment continued until confirmed radiographic progression, unacceptable toxicity, investigator decision, participant withdrawal of

consent or a maximum of 12 months, extended to 24 months in September 2017 for alignment with the therapeutic landscape at the time. Therapy response was assessed by overall response rate at 12 weeks using RECIST 1.1. Tumors with radiographic CR or partial response (PR) were classified as responding, while tumors with radiographic stable disease (SD) or progressive disease (PD) were classified as nonresponding. PFS and OS, estimated from time of trial enrollment to progression or status at last follow-up, respectively, according to a data cutoff date of April 16, 2024, were used to capture long-term clinical outcomes. Two participants in the control arm experienced progression at week 6 followed by PR at week 12, which was considered pseudoprogression (as described in the original trial) and this was reflected in the therapy response assignments[13]. Participants attaining an OS of at least 3 years from time of trial enrollment were classified in the long-term response group (12 in the control arm and 8 in the SBRT arm). Clinical data collection and clinical trial endpoint determination were performed independent of the conditions of the experiments.

We leveraged 293 serial tumor and peripheral blood samples collected at baseline and after two cycles of pembrolizumab from 72 participants in the control ($n = 37$) and SBRT ($n = 35$) arms, for which biospecimens were procured. Tumor biopsies were serially obtained from a nonirradiated tumor lesion and matched baseline and on-therapy tumor and blood samples were used for genomic, transcriptomic and immunologic analyses. TMB-low (<300 mutations per exome; $n = 43$), PDL1-null (0% expression on IHC; $n = 41$) or Wnt-mutated (presence of mutations affecting genes in the Wnt pathway; $n = 10$) tumors were defined as immunologically cold. A cutoff of 300 mutations per exome was selected to optimize the difference in both PFS and OS between the TMB-low and TMB-high groups across the cohort.

WES
We performed WES on 116 samples (58 tumor–normal pairs) from 30 participants treated with pembrolizumab monotherapy (control) and 28 participants treated with SBRT followed by pembrolizumab (SBRT) (Supplementary Table 1). DNA was extracted from baseline tumor and matched peripheral blood samples, fragmented and used to prepare WES libraries with the Illumina TruSeq library kit. Exonic regions were captured in solution using the Agilent SureSelect v4 kit, followed by paired-end sequencing using Illumina HiSeq 2000/2500 instruments[17,44,45]. The mean depth of total and distinct coverage was 207× and 160× for tumor and 91× and 78× for normal samples, respectively (Supplementary Table 1). WES data were processed to identify somatic variants using VariantDx[44,45] (Supplementary Table 2). Recurring mutations with a frequency of 10 or higher in the COSMIC[46] database (version 100; https://cancer.sanger.ac.uk/cosmic/login) were considered cancer hotspots.

Mutation signature analysis
Mutation signatures were based on the fraction of coding point mutations in each of 96 trinucleotide contexts and the contribution of each signature to each tumor sample was estimated using the deconstructSigs R package (version 1.8.0) with the default 'signatures.nature2013' settings (https://cran.r-project.org/package=deconstructSigs) (Supplementary Table 5).

Aneuploidy assessment
We used FACETS 0.6.1 for assessing the purity of individual tumor samples, generating integer allele-specific copy-number profiles across the entire genome and determining the cellular fraction associated with each aberrant somatic copy-number alteration[47]. The extent of genome aneuploidy was estimated by the proportion of the genome with allelic imbalance[17] and several additional metrics (ploidy, entropy, modal ploidy, nonmodal genome fraction, fraction of the genome with loss of heterozygosity and nondiploid genome fraction) (Supplementary Tables 5 and 6). To directly compare aneuploidy analyses in the

PEMBRO-RT cohort with previously published studies[18], we computed ASCETS aneuploidy scores per tumor sample and compared ASCETS scores between responding and nonresponding tumors.

RNA-seq, differential expression and enrichment analysis

We analyzed 48 tumor samples from 12 participants treated with pembrolizumab (12 baseline and 10 on therapy) and 16 participants treated with SBRT followed by pembrolizumab (14 baseline and 12 on therapy) (Supplementary Table 3). Total RNA was extracted from 10-μm formalin-fixed paraffin-embedded (FFPE) sections using the RNeasy FFPE kit (Qiagen). The quality of the obtained total RNA was evaluated by calculating the DV200 index, measured with the RNA 6000 Pico kit (Agilent Technologies). RNA-seq libraries were constructed through poly(A) selection (NEBNext poly(A) isolation kit) followed by reverse transcription to generate strand-specific complementary DNA libraries (NEBNext Ultra Directional RNA library prep kit for Illumina). Subsequently, paired-end sequencing (150 bp) was performed using Illumina NovaSeq 6000 S4, resulting in an average of 200 million total reads per library. RNA-seq data were aligned to the human transcriptome using STAR-2.7.3a (ref. 48), followed by RSEM-1.2.30 for isoform and gene-level quantification[49]. Transcripts associated with RNA genes, mitochondrial genes and ribosomal proteins were masked during the analysis. Sample-level quality control was performed using the total count, number of counts aligned to the genome, number of counts aligned to the transcriptome and percentage of reads aligning to the transcriptome for each sample. The batch effect was evaluated using both principal component analysis and correlation across the entire transcriptome in conjunction with universal human reference samples sequenced in each batch. Normalization of raw transcript counts and differential expression analysis were performed with DESeq2 1.42.0 (ref. 50) and the resulting P values were corrected for multiple testing using the Benjamini–Hochberg procedure. Normalized gene expression counts were analyzed with the fgsea48 (version 1.20.0)[51] R package for GSEA with a preselected suite of gene sets (Supplementary Table 32), with resulting P values corrected for multiple testing. Genes that passed the count threshold were ranked by $-\log(P \text{ value}) \times \text{sign(FC)}$, where FC is the fold change. For TLS GSEA analyses, the TLS gene set included the following genes: *MS4A1*, *CD4*, *MKI67*, *AICDA*, *MADCAM1*, *IL33*, *CDR2*, *CD40*, *CXCR5*, *LTB*, *CXCL13*, *CCL19*, *SELL*, *CCR7*, *CXCR4* and *CCL5*.

RNA-seq deconvolution

We used CIBERSORT (version 1.06)[52] to perform deconvolution of transcriptome data, producing relative and absolute proportion estimates for 22 immune cell types. CIBERSORT uses a deconvolution-based approach with a reference gene signature matrix to assess the proportion of each immune cell type within the total immune cells present in the mixture. In our differential abundance analyses, we used the absolute abundance measurements of immune cell subsets. We used TRUST4 to reconstruct the BCR repertoires from transcriptomic data and better estimate B cell diversity and BCR repertoire at the specific BCR clonotype level[53]. We compared B cell densities between baseline and on-therapy tumors and by treatment arms and radiographic response.

TCR sequencing and enrichment analyses

TCR CDR3Vb sequencing was performed using serial peripheral blood and tumor tissue samples; we analyzed 129 samples from 31 participants (18 in the SBRT arm and 13 in the control arm), consisting of 64 blood samples (31 baseline, 31 on therapy and 2 resistance) and 65 tumor samples (31 baseline, 31 on therapy and 3 resistance) (Supplementary Table 4). DNA from baseline tumor and blood samples was isolated with Qiagen DNA FFPE and Qiagen DNA blood mini kits. TCR CDR3β regions were amplified using the ImmunoSeq survey assay with multiplex PCR using 45 forward primers to specific Vβ segments

and 13 reverse primers to specific Jβ segments (Adaptive Biotechnologies)[54]. TCR sequences representing in-frame productive clones were further analyzed according to their CDR3 amino acid sequences. For each participant, clones achieving at least 0.05% relative abundance were included for differential abundance analysis between baseline and on-therapy time points in tumor and blood specimens. To conduct a differential abundance analysis between baseline and on-therapy tumors, we identified the most expanded and most regressed TCR clonotypes. These were determined on the basis of FC in the productive frequency of TCR clones, only counting clones with an FDR-adjusted P value < 0.05 (Mann–Whitney U-test). Aggregated clone counts with significant expansion dynamics (increasing or decreasing) between baseline and on-therapy samples (in tumor and/or blood) were collated and compared across participants by response and treatment categories using GLMs. Counts of expanded TCR clones were obtained in three compartments: tumor but not blood, blood but not tumor and both settings. For each compartment, association between clone count and treatment group was assessed using GLMs. Two sets of analyses were performed for each compartment, first including all clones that expanded on treatment (any level of pretreatment abundance) and then including only those clones that expanded on treatment but were not found in baseline samples (pretreatment abundance of 0, 'newly expanded clones'). To adjust for TMB and PDL1 status, these variables were included in the GLM.

Functional T cell assays

We selected clonal expressed mutations detected at abscopal (biopsied) sites from three participants with radiographic responses and long-term OS in the SBRT arm and tested for neoantigen-reactive T cell responses in autologous T cells using the MANAFEST assay, which detects neoantigen-reactive T cell expansions with high sensitivity and specificity[21,44]. This approach combines ex vivo T cell culture and peptide stimulation with TCR sequencing to identify neoantigen-reactive T cell clonotypic expansions induced by neoantigens. From each participant, 7–13 somatic mutations were selected on the basis of predicted MHC class I binding rank of associated neoantigens, expression in participant-matched RNA-seq data, mutation clonality and mutation type (insertions and deletions that satisfied previous criteria were prioritized when present). Peptides containing the mutation were synthesized and are listed in Supplementary Table 28 (GenScript). T cells were isolated from peripheral blood mononuclear cells (PBMCs) by negative selection (EasySep; StemCell Technologies) from baseline, cycle 2 day 1, cycle 3 day 1 and cycle 4 day 1, cultured and stimulated in separate wells with each of the synthesized neopeptides[21,44]. TCR sequencing of extracted DNA from cultured CD8+ cells was performed by the Johns Hopkins Fest and TCR Immunogenomics Core Facility using the AmpliSeq for Illumina TCR beta-SR assay. Nonproductive TCR sequences were eliminated and aligned to obtain only the CDR3 region. Sequences not beginning with C or ending with F or W and having fewer than seven amino acids were eliminated. For singlet analyses performed for participant CGLU680 (Supplementary Table 29), processed data files were analyzed using the publicly available MANAFEST analysis web application (http://www.stat-apps.onc.jhmi.edu/FEST) to define neoantigen-specific T cell clonotypes. For participants CGLU690 and CGLU727, for whom adequate numbers of PBMCs were available for triplicate analyses, we analyzed TCR clone abundances per subject time points across peptide stimulation configurations. Multiple replicates per configuration were evaluated by (1) determining the set of TCR clones that were positive in the majority of replicates available for a given configuration and (2) determining clones at least fivefold greater in percentage abundance in the target condition (as measured by the lowest positive value) than the next highest single replicate from a different configuration. This procedure was performed for each time point within each participant separately (Supplementary Tables 30 and 31).

Statistical analysis and reproducibility

The progression-free interval was defined as the time from diagnosis to disease progression or death. Median point estimates and 95% confidence intervals for PFS and OS were calculated using the Kaplan–Meier method and survival curves were compared using the nonparametric log-rank test. Differences in genomic and transcriptomic features between responding and nonresponding tumors were assessed using the Fisher's exact test for categorical variables and the Mann–Whitney test for continuous variables. P values were corrected using the Benjamini–Hochberg procedure and the FDR values were calculated. We further conducted multivariate Cox proportional hazards regression analyses to assess the independent association between SBRT therapy and PFS and OS in immunologically cold tumors while controlling for potential confounding variables (age, sex, tumor histology, smoking status and tumor purity). Statistical analyses were conducted using R version 3.6 and higher (http://cran.r-project.org). Nonparametric tests were used and, thus, data distribution was not tested for normality. No statistical methods were used to predetermine sample sizes but our sample sizes are similar to those reported in previous publications[17]. Randomization was not applicable for the exploratory multiomic analyses reported in this study. In the PEMBRO-RT study, participants were randomly assigned using a 1:1 ratio to receive treatment with pembrolizumab either after SBRT to a single tumor site (experimental arm) or without SBRT (control arm). While blinding is not entirely relevant outside the context of a clinical trial, clinical data collection and clinical trial endpoint determination were performed independent of the conditions of the experiments.

Reporting summary

Further information on research design is available in the Nature Portfolio Reporting Summary linked to this article.

Data availability

WES and RNA-seq data were deposited to the European Genome-Phenome Archive (EGA) under accession numbers EGAS50000000277 and EGAD50000000404. The following data use ontologies are linked with the EGA dataset EGAD50000000404, related to privacy restrictions included in the informed consent: not for profit, noncommercial use only, indicating that the data are limited to not-for-profit organizations and not for profit, noncommercial use; institutional review board (IRB) ethics approval required, indicating that the requestor must provide documentation of local institutional or ethics review board approval; user-specific restriction, indicating that use is limited to use by approved users; project-specific restriction, indicating that use is limited to use within an approved project. Requests for access to the sequence data can be submitted in the EGA portal using the access codes above, after which the requestor will receive a data access agreement that needs to be filled in with respect to description of the research in which the dataset will be used. Commercial or for-profit use of the dataset is not allowed per regulatory mandates and the requestor must provide documentation of local IRB approval. Following review and sign off by the requestor and the requestor's institution regulatory official, the data access agreement will be reviewed by the Office of Research Administration at Johns Hopkins University. Following review, the agreement will be signed and sent back to the requestor. Following completion of the process above, the dataset will be released to the requestor in EGA. The timeline for the above process depends on the speed of regulatory review required. Clinical data are available upon request from W.S.M.E.T. at the Netherlands Cancer Institute (w.theelen@nki.nl). Source data are provided with this paper.

Code availability

All computational pipelines used in this work are explicitly described and referenced in Methods. No custom code was used for this work.

References

1. Demaria, S., Golden, E. B. & Formenti, S. C. Role of local radiation therapy in cancer immunotherapy. *JAMA Oncol.* **1**, 1325–1332 (2015).
2. Kroemer, G., Galassi, C., Zitvogel, L. & Galluzzi, L. Immunogenic cell stress and death. *Nat. Immunol.* **23**, 487–500 (2022).
3. McLaughlin, M. et al. Inflammatory microenvironment remodelling by tumour cells after radiotherapy. *Nat. Rev. Cancer* **20**, 203–217 (2020).
4. Formenti, S. C. & Demaria, S. Systemic effects of local radiotherapy. *Lancet Oncol.* **10**, 718–726 (2009).
5. Rodriguez-Ruiz, M. E. et al. Abscopal effects of radiotherapy are enhanced by combined immunostimulatory mAbs and are dependent on CD8 T cells and crosspriming. *Cancer Res.* **76**, 5994–6005 (2016).
6. Demaria, S. et al. Immune-mediated inhibition of metastases after treatment with local radiation and CTLA-4 blockade in a mouse model of breast cancer. *Clin. Cancer Res.* **11**, 728–734 (2005).
7. Laurent, P.-A., Morel, D., Meziani, L., Depil, S. & Deutsch, E. Radiotherapy as a means to increase the efficacy of T-cell therapy in solid tumors. *Oncoimmunology* **12**, 2158013 (2023).
8. Wei, J. et al. Sequence of αPD-1 relative to local tumor irradiation determines the induction of abscopal antitumor immune responses. *Sci. Immunol.* **6**, eabg0117 (2021).
9. Rudqvist, N.-P. et al. Immunotherapy targeting different immune compartments in combination with radiation therapy induces regression of resistant tumors. *Nat. Commun.* **14**, 5146 (2023).
10. Rodriguez-Ruiz, M. E., Vitale, I., Harrington, K. J., Melero, I. & Galluzzi, L. Immunological impact of cell death signaling driven by radiation on the tumor microenvironment. *Nat. Immunol.* **21**, 120–134 (2020).
11. Ngwa, W. et al. Using immunotherapy to boost the abscopal effect. *Nat. Rev. Cancer* **18**, 313–322 (2018).
12. Galluzzi, L., Aryankalayil, M. J., Coleman, C. N. & Formenti, S. C. Emerging evidence for adapting radiotherapy to immunotherapy. *Nat. Rev. Clin. Oncol.* **20**, 543–557 (2023).
13. Theelen, W. S. M. E. et al. Effect of pembrolizumab after stereotactic body radiotherapy vs pembrolizumab alone on tumor response in patients with advanced non-small cell lung cancer: results of the PEMBRO-RT phase 2 randomized clinical trial. *JAMA Oncol.* **5**, 1276–1282 (2019).
14. Formenti, S. C. et al. Radiotherapy induces responses of lung cancer to CTLA-4 blockade. *Nat. Med.* **24**, 1845–1851 (2018).
15. Ohri, N. et al. Selective personalized radioimmunotherapy for locally advanced non-small-cell lung cancer trial. *J. Clin. Oncol.* **42**, 562–570 (2024).
16. Altorki, N. K. et al. Neoadjuvant durvalumab with or without stereotactic body radiotherapy in patients with early-stage non-small-cell lung cancer: a single-centre, randomised phase 2 trial. *Lancet Oncol.* **22**, 824–835 (2021).
17. Anagnostou, V. et al. Multimodal genomic features predict outcome of immune checkpoint blockade in non-small-cell lung cancer. *Nat. Cancer* **1**, 99–111 (2020).
18. Spurr, L. F. et al. Highly aneuploid non-small cell lung cancer shows enhanced responsiveness to concurrent radiation and immune checkpoint blockade. *Nat. Cancer* **3**, 1498–1512 (2022).
19. Scharpf, R. B. et al. Genomic landscapes and hallmarks of mutant RAS in human cancers. *Cancer Res.* **82**, 4058–4078 (2022).
20. Spranger, S., Bao, R. & Gajewski, T. F. Melanoma-intrinsic β-catenin signalling prevents anti-tumour immunity. *Nature* **523**, 231–235 (2015).
21. Danilova, L. et al. The mutation-associated neoantigen functional expansion of specific T cells (MANAFEST) assay: a sensitive platform for monitoring antitumor immunity. *Cancer Immunol. Res.* **6**, 888–899 (2018).

22. Theelen, W. et al. Pembrolizumab with or without radiotherapy for metastatic non-small-cell lung cancer: a pooled analysis of two randomised trials. *Lancet Respir. Med.* **9**, 467–475 (2021).

23. Schoenfeld, J. D. et al. Durvalumab plus tremelimumab alone or in combination with low-dose or hypofractionated radiotherapy in metastatic non-small-cell lung cancer refractory to previous PD(L)-1 therapy: an open-label, multicentre, randomised, phase 2 trial. *Lancet Oncol.* **23**, 279–291 (2022).

24. Peters, S. et al. Progression-free and overall survival for concurrent nivolumab with standard concurrent chemoradiotherapy in locally advanced stage IIIA–B NSCLC: results from the European thoracic oncology platform NICOLAS phase II trial (European Thoracic Oncology Platform 6-14). *J. Thorac. Oncol.* **16**, 278–288 (2021).

25. Spigel, D. R. et al. Five-year survival outcomes from the PACIFIC trial: durvalumab after chemoradiotherapy in stage III non-small-cell lung cancer. *J. Clin. Oncol.* **40**, 1301–1311 (2022).

26. van der Woude, L. L. et al. Tumor microenvironment shows an immunological abscopal effect in patients with NSCLC treated with pembrolizumab–radiotherapy combination. *J. Immunother. Cancer* **10**, e005248 (2022).

27. Golden, E. B. et al. Radiation fosters dose-dependent and chemotherapy-induced immunogenic cell death. *Oncoimmunology* **3**, e28518 (2014).

28. Burnette, B. C. et al. The efficacy of radiotherapy relies upon induction of type I interferon-dependent innate and adaptive immunity. *Cancer Res.* **71**, 2488–2496 (2011).

29. Reits, E. A. et al. Radiation modulates the peptide repertoire, enhances MHC class I expression, and induces successful antitumor immunotherapy. *J. Exp. Med.* **203**, 1259–1271 (2006).

30. Dovedi, S. J. et al. Acquired resistance to fractionated radiotherapy can be overcome by concurrent PD-L1 blockade. *Cancer Res.* **74**, 5458–5468 (2014).

31. Matsumura, S. et al. Radiation-induced CXCL16 release by breast cancer cells attracts effector T cells. *J. Immunol.* **181**, 3099–3107 (2008).

32. Galluzzi, L., Kepp, O., Hett, E., Kroemer, G. & Marincola, F. M. Immunogenic cell death in cancer: concept and therapeutic implications. *J. Transl. Med.* **21**, 162 (2023).

33. Theelen, W. S., de Jong, M. C. & Baas, P. Synergizing systemic responses by combining immunotherapy with radiotherapy in metastatic non-small cell lung cancer: the potential of the abscopal effect. *Lung Cancer* **142**, 106–113 (2020).

34. Grass, G. D., Krishna, N. & Kim, S. The immune mechanisms of abscopal effect in radiation therapy. *Curr. Probl. Cancer* **40**, 10–24 (2016).

35. Voong, K. R. et al. Ablative radiation alone in stage I lung cancer produces an adaptive systemic immune response: insights from a prospective study. *J. Immunother. Cancer* **11**, e007188 (2023).

36. Anagnostou, V., Landon, B. V., Medina, J. E., Forde, P. & Velculescu, V. E. Translating the evolving molecular landscape of tumors to biomarkers of response for cancer immunotherapy. *Sci. Transl. Med.* **14**, eabo3958 (2022).

37. Spranger, S. & Gajewski, T. F. Impact of oncogenic pathways on evasion of antitumour immune responses. *Nat. Rev. Cancer* **18**, 139–147 (2018).

38. Tumeh, P. C. et al. PD-1 blockade induces responses by inhibiting adaptive immune resistance. *Nature* **515**, 568–571 (2014).

39. Sundahl, N. et al. Phase 2 trial of nivolumab combined with stereotactic body radiation therapy in patients with metastatic or locally advanced inoperable nelanoma. *Int. J. Radiat. Oncol. Biol. Phys.* **104**, 828–835 (2019).

40. McBride, S. et al. Randomized phase II trial of nivolumab with stereotactic body radiotherapy versus nivolumab alone in metastatic head and neck squamous cell carcinoma. *J. Clin. Oncol.* **39**, 30–37 (2021).

41. Masini, C. et al. Nivolumab in combination with stereotactic body radiotherapy in pretreated patients with metastatic renal cell carcinoma. Results of the phase II NIVES study. *Eur. Urol.* **81**, 274–282 (2022).

42. Spaas, M. et al. Checkpoint inhibitors in combination with stereotactic body radiotherapy in patients with advanced solid tumors: the CHEERS phase 2 randomized clinical trial. *JAMA Oncol.* **9**, 1205–1213 (2023).

43. Harding, S. M. et al. Mitotic progression following DNA damage enables pattern recognition within micronuclei. *Nature* **548**, 466–470 (2017).

44. Anagnostou, V. et al. Evolution of neoantigen landscape during immune checkpoint blockade in non-small cell lung cancer. *Cancer Discov.* **7**, 264–276 (2017).

45. Jones, S. et al. Personalized genomic analyses for cancer mutation discovery and interpretation. *Sci. Transl. Med.* **7**, 283ra253 (2015).

46. Tate, J. G. et al. COSMIC: the Catalogue Of Somatic Mutations In Cancer. *Nucleic Acids Res.* **47**, D941–D947 (2019).

47. Shen, R. & Seshan, V. E. FACETS: allele-specific copy number and clonal heterogeneity analysis tool for high-throughput DNA sequencing. *Nucleic Acids Res.* **44**, e131 (2016).

48. Dobin, A. & Gingeras, T. R. Mapping RNA-seq reads with STAR. *Curr. Protoc. Bioinformatics* **51**, 11.14.11–11.14.19 (2015).

49. Li, B. & Dewey, C. N. RSEM: accurate transcript quantification from RNA-seq data with or without a reference genome. *BMC Bioinformatics* **12**, 323 (2011).

50. Love, M. I., Huber, W. & Anders, S. Moderated estimation of fold change and dispersion for RNA-seq data with DESeq2. *Genome Biol.* **15**, 550 (2014).

51. Korotkevich, G. et al. Fast gene set enrichment analysis. Preprint at *bioRxiv* https://doi.org/10.1101/060012 (2021).

52. Newman, A. M. et al. Robust enumeration of cell subsets from tissue expression profiles. *Nat. Methods* **12**, 453–457 (2015).

53. Song, L. et al. TRUST4: immune repertoire reconstruction from bulk and single-cell RNA-seq data. *Nat. Methods* **18**, 627–630 (2021).

54. Carlson, C. S. et al. Using synthetic templates to design an unbiased multiplex PCR assay. *Nat. Commun.* **4**, 2680 (2013).

Author contributions

V.A., Z.B., W.S.M.E.T. and J.H. conceptualized the study and contributed to the study design, data analysis, data interpretation and writing. A.B., C.C., J.R.W., D.S., J.H., J.W., M.N. and N.N. contributed to data analysis. M.N. and J.H. contributed to writing. D.v.d.G., J.H., R.K., M.M.v.d.H., K.N.S., P.B. and V.E.V. contributed to data collection and/or interpretation and edited the paper.

Competing interests

V.A. receives research funding to Johns Hopkins University from Astra Zeneca and Personal Genome Diagnostics, has received research funding to Johns Hopkins University from Bristol-Myers Squibb and Delfi Diagnostics in the past 5 years, is an advisory board member for Astra Zeneca and Neogenomics (compensated), and receives honoraria from Foundation Medicine, Guardant Health and Personal Genome Diagnostics; these arrangements have been reviewed and approved by Johns Hopkins University in accordance with its conflict-of-interest policies. V.A. is an inventor on patent applications

Additional information

Extended data is available for this paper at https://doi.org/10.1038/s43018-025-01018-w.

Supplementary information The online version contains supplementary material available at https://doi.org/10.1038/s43018-025-01018-w.

Correspondence and requests for materials should be addressed to Valsamo Anagnostou.

Peer review information *Nature Cancer* thanks Aadel Chaudhuri, John Minna and Narek Shaverdian for their contribution to the peer review of this work.

Reprints and permissions information is available at www.nature.com/reprints.

[1]The Sidney Kimmel Comprehensive Cancer Center, Johns Hopkins University School of Medicine, Baltimore, MD, USA. [2]Netherlands Cancer Institute, Amsterdam, The Netherlands. [3]The Bloomberg~Kimmel Institute for Cancer Immunotherapy, Johns Hopkins University School of Medicine, Baltimore, MD, USA. [4]Institute for Computational Medicine, Johns Hopkins University, Baltimore, MD, USA. [5]Department of Pulmonary Diseases, Radboud University Medical Center, Nijmegen, The Netherlands. [6]These authors contributed equally: Justin Huang, Willemijn S. M. E. Theelen, Zineb Belcaid. ✉e-mail: vanagno1@jhmi.edu

a

b

c

d
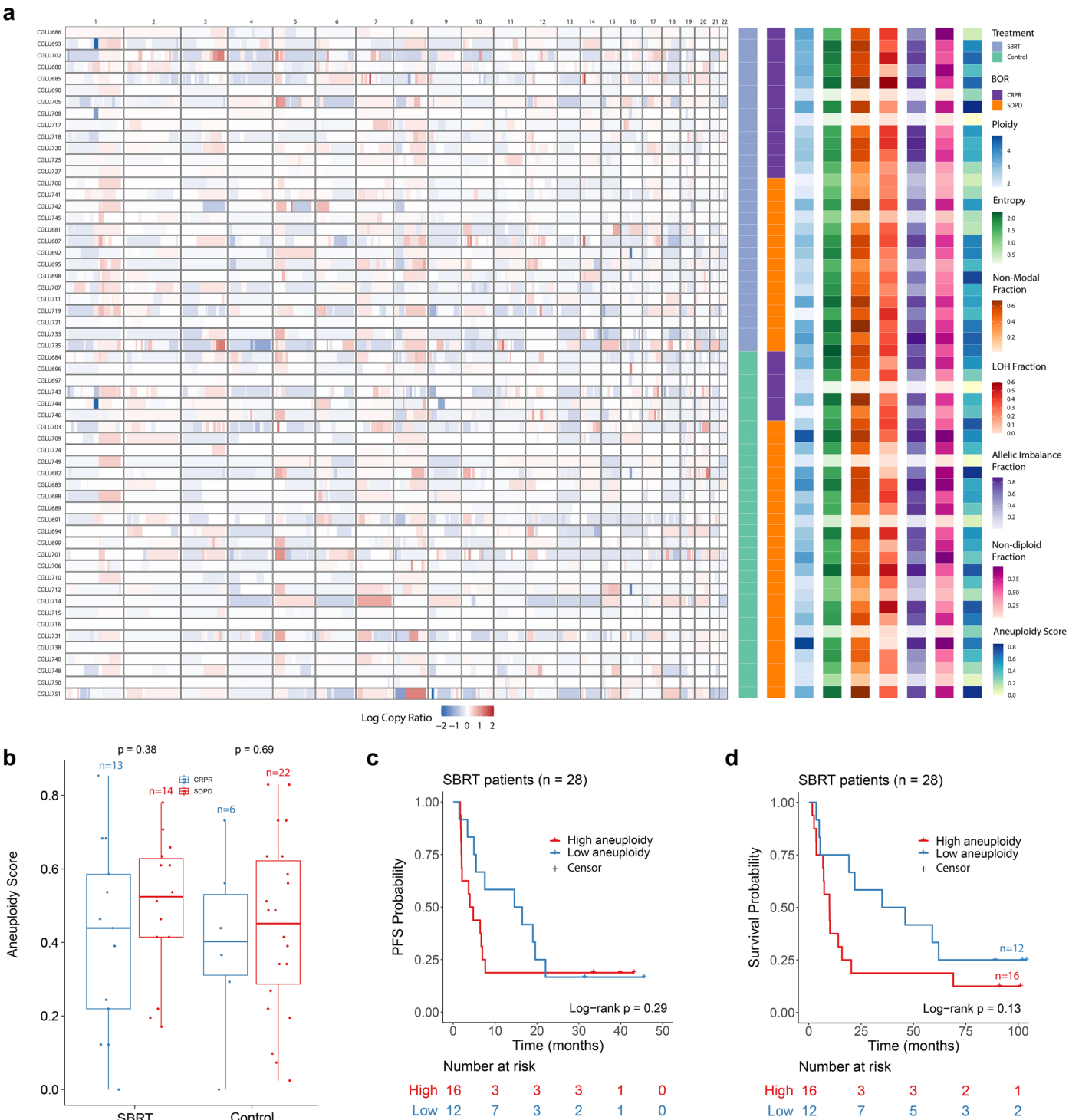
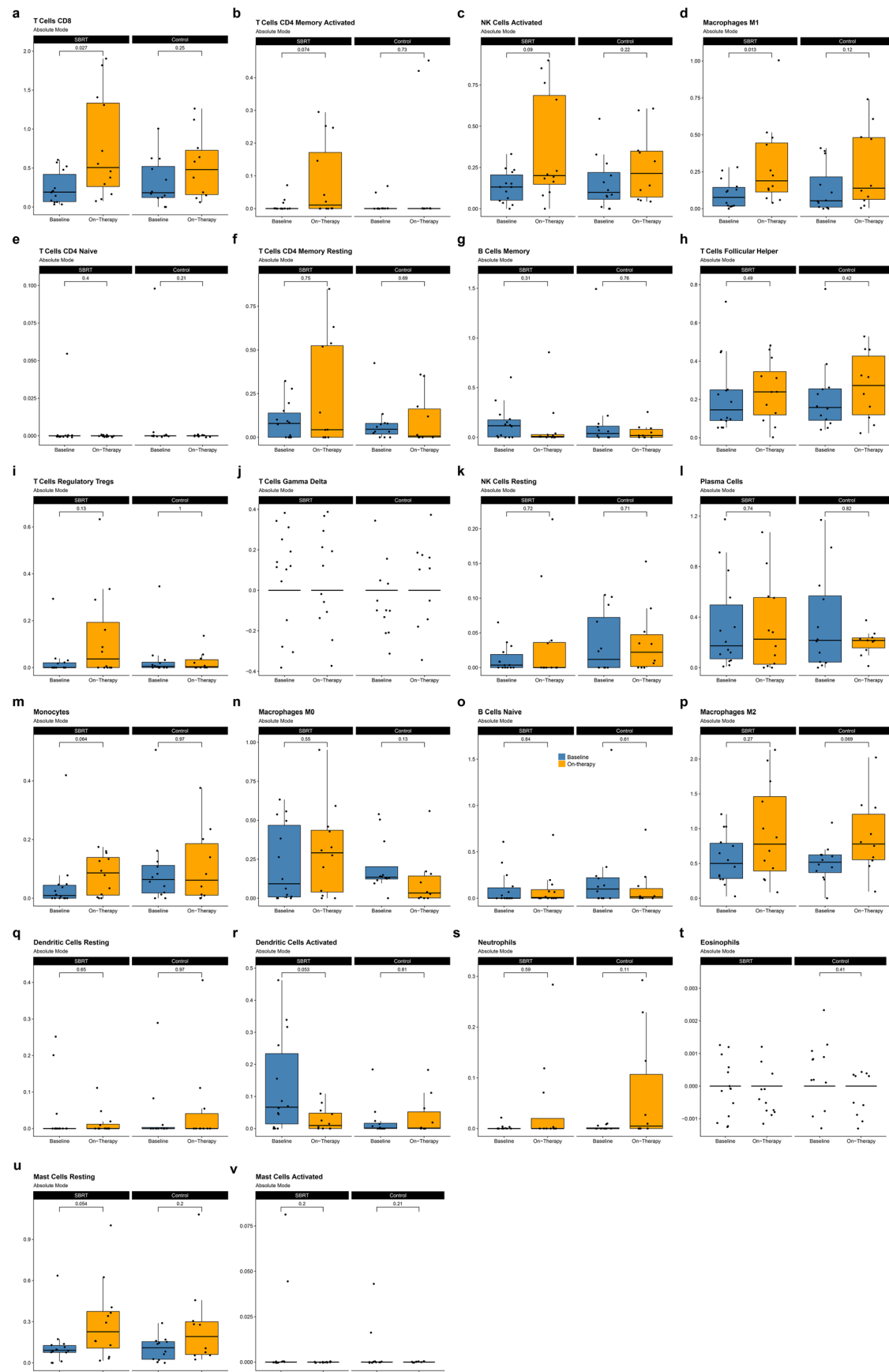**Extended Data Fig. 1 | See next page for caption.**

Extended Data Fig. 1 | Tumor aneuploidy shows variable correlation with response in patients in the SBRT arm depending on the aneuploidy metric used. (**a**) Copy number ratios and aneuploidy scores across all patients. There was no significant difference between responders and non-responders in the SBRT cohort for any of the seven metrics (ploidy SBRT responders mean = 2.82, SBRT non-responders mean = 2.72, Mann-Whitney U test two-sided P = 0.68; entropy SBRT responders mean = 1.50, SBRT non-responders mean = 1.74, Mann-Whitney U test two-sided P = 0.52; non modal fraction SBRT responders mean = 0.45, SBRT non-responders mean = 0.48, Mann-Whitney U test two-sided P = 0.87; loss of heterozygosity fraction SBRT responders mean = 0.28, SBRT non-responders mean = 0.30, Mann-Whitney U test two-sided P = 0.79; genomic imbalance fraction SBRT responders mean = 0.56, SBRT non-responders mean = 0.58, Mann-Whitney U test two-sided P = 0.83; nondiploid fraction SBRT responders mean = 0.53, SBRT non-responders mean = 0.53, Mann-Whitney U test two-sided P = 0.87; ASCETS score SBRT responders mean = 0.41, SBRT non-responders mean = 0.49, Mann-Whitney U test two-sided P = 0.38) (**b**) Comparison of ASCETS score between responders (CR or PR) and non-responders (SD or PD) in each therapy arm. There was no difference in

ASCETS score between response groups in either arm (SBRT results reported under (**a**); control responders mean = 0.40, control non-responders mean = 0.45, Mann-Whitney U test two-sided P = 0.69). Box plots depict the median value and hinges correspond to the first and third quartiles. The whiskers extend from the corresponding hinge to the furthest value within 1.5* the interquartile range from the hinge. (**c**) Kaplan-Meier analyses for PFS in SBRT patients with whole exome sequencing data (n = 28 patients) who were classified according to the Spurr et al. paper as high aneuploidy (ASCETS > = 0.42, n = 16 patients) versus low aneuploidy (ASCETS < 0.42, n = 12 patients) showed a numerically shorter PFS for patients with highly aneuploid tumors (median PFS high aneuploidy 4.39 months vs low aneuploidy 15.56 months, log-rank P = 0.29). (**d**) Kaplan-Meier analyses for OS in SBRT patients with whole exome sequencing data (n = 28 patients) who were classified according to the Spurr et al. paper as high aneuploidy (ASCETS > = 0.42, n = 16 patients) versus low aneuploidy (ASCETS < 0.42, n = 12 patients) revealed a numerically shorter OS in the high aneuploidy group which was statistically insignificant (median OS high aneuploidy 9.89 months vs low aneuploidy 40.50 months, log-rank P = 0.13).
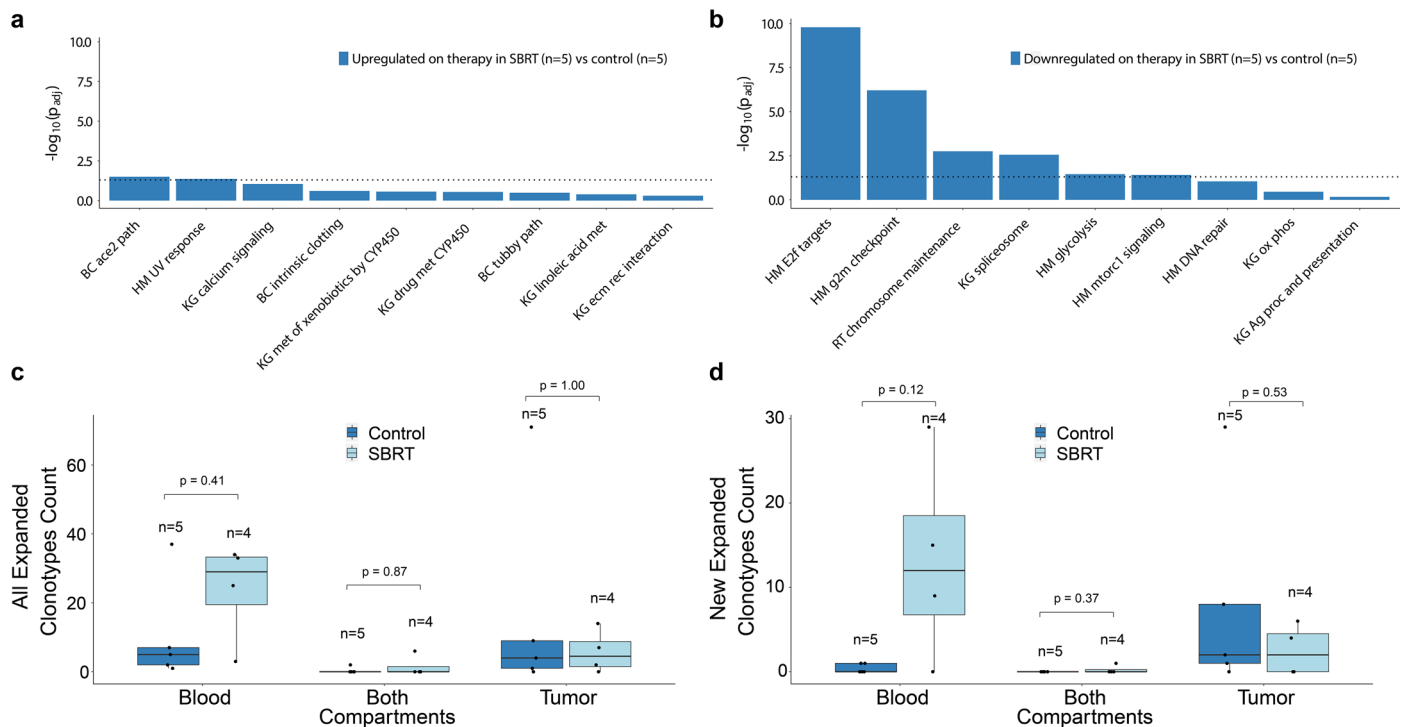
Extended Data Fig. 2 | Patients with STK11 mutated tumors in the SBRT and control arms show no difference in upregulation of immune programs or T cell expansion. (**a**) We did not observe significant upregulation of immune response related gene sets in on-therapy tumors among patients with STK11 mutations in the SBRT arm (n = 5 samples) versus the control arm (n = 5 samples). (**b**) Among patients with STK11 mutations, cellular proliferation and cell cycle progression gene sets were significantly more downregulated in on-therapy tumors in the SBRT (n = 5 samples) compared to the control arm (n = 5 samples; E2f targets, GSEA (two-sided) FDR-adjusted P = 1.62e-10, NES = −2.33; g2m checkpoint, GSEA (two-sided) FDR-adjusted P = 6.14e-7, NES = −2.07). (c, d) There were no significant differences in T cell expansion between patients with STK11 mutations in the SBRT (n = 4 samples) and control (n = 5 samples) arms for all clones (**c**) or only newly expanded clones (**d**) (Mann-Whitney U test, two-sided). While limited by the small number of STK11-mutant tumors per arm, these findings do not support an enhancement of anti-tumor immune responses in the SBRT arm compared to the control arm for tumors harboring STK11 mutations. Box plots depict the median value and hinges correspond to the first and third quartiles. The whiskers extend from the corresponding hinge to the furthest value within 1.5* the interquartile range from the hinge.

**Extended Data Fig. 3 | See next page for caption.**

Extended Data Fig. 3 | Differences in absolute abundance of immune cell subsets derived from RNAseq deconvolution from baseline to on-therapy in the SBRT and control groups. (a–v) A significantly greater abundance of CD8 T cells (mean SBRT baseline 0.244, mean SBRT on-therapy 0.765, Mann Whitney-U test (two-sided) P = 0.027) and M1 macrophages (mean SBRT baseline 0.099, mean SBRT on-therapy 0.292, Mann Whitney-U test (two-sided) P = 0.013) were noted on-therapy in the SBRT arm. We also observed a trend towards a higher abundance of activated CD4 memory T cells (mean SBRT baseline 0.008, mean SBRT on-therapy 0.083, Mann Whitney-U test (two-sided) P = 0.074) and activated NK cells (mean SBRT baseline 0.134, mean SBRT on-therapy 0.361, Mann Whitney-U test (two-sided) P = 0.090) on-therapy compared to baseline in the SBRT arm. These differences were less pronounced in the control arm (CD8 T cells mean control baseline 0.320, mean control on-therapy 0.525, Mann Whitney-U test (two-sided) P = 0.248; activated CD4 memory T cells mean control baseline 0.010, mean control on-therapy 0.087, Mann Whitney-U test (two-sided) P = 0.732; activated NK cells mean control baseline 0.156, mean control on-therapy 0.259, Mann Whitney-U test (two-sided) P = 0.222; M1 macrophages mean control baseline 0.135, mean control on-therapy 0.275, Mann Whitney-U test (two-sided) P = 0.121). A trend towards a higher abundance of M2 macrophages in on-therapy compared to baseline samples was noted in the control group, while such a difference was not noted in the SBRT group (mean control baseline 0.506, mean control on-therapy 0.883, Mann Whitney-U test (two-sided) P = 0.069; mean SBRT baseline 0.562, mean SBRT on-therapy 0.943, Mann Whitney-U test (two-sided) P = 0.274). Absolute abundance values and statistics related to all other cell types determined by RNA-seq deconvolution are listed in Supplementary Table 12. Sample sizes for all panels are: SBRT Baseline n = 14 samples, SBRT on-therapy n = 12 samples, control baseline n = 12 samples, control on-therapy n = 10 samples. Box plots depict the median value and hinges correspond to the first and third quartiles. The whiskers extend from the corresponding hinge to the furthest value within 1.5* the interquartile range from the hinge.
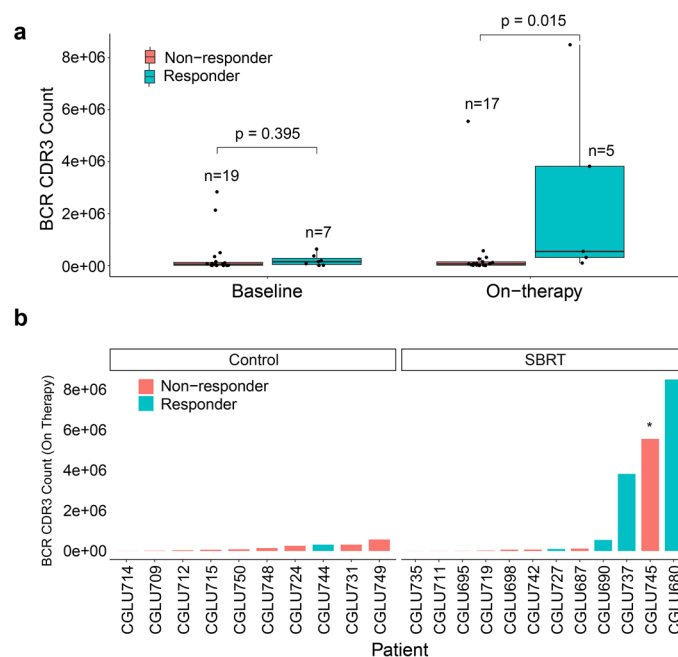
Extended Data Fig. 4 | B cell expansion is associated with improved response, with notably greater expansion observed in a subset of patients in the SBRT arm. (**a**) B cell CDR3 count at baseline was similar between responders and non-responders (mean 3.39e5 non-responders, 2.03e5 responders, Mann-Whitney U test (two-sided) P = 0.395), but significantly greater on-therapy in responders (mean 0.429e6 non-responders, 2.65e6 responders, Mann-Whitney U test (two-sided) P = 0.015). Non-responding tumors showed no difference in BCR CDR3 count between baseline and on-therapy samples in the control [mean 3.30e5 vs 1.63e5, Mann-Whitney U test (two-sided) P = 0.97] or SBRT arms [mean 3.46e5 vs 7.28e5, Mann-Whitney U test (two-sided) P = 0.74].

Box plots depict the median value and hinges correspond to the first and third quartiles. The whiskers extend from the corresponding hinge to the furthest value within 1.5* the interquartile range from the hinge. (**b**) B cell CDR3 count on-therapy for each patient with RNAseq data available, with 3 patients in the SBRT arm (CGLU737, CGLU745, CGLU680) demonstrating notably greater B cell count on-therapy than any patient in the control arm. Of note, although CGLU745 is a radiographic non-responder (stable disease), this patient also experienced a durable response (durable clinical benefit, PFS 7.6 months, OS 35 months, compared to average PFS of 3.8 months and OS of 10.6 months among non-responders).
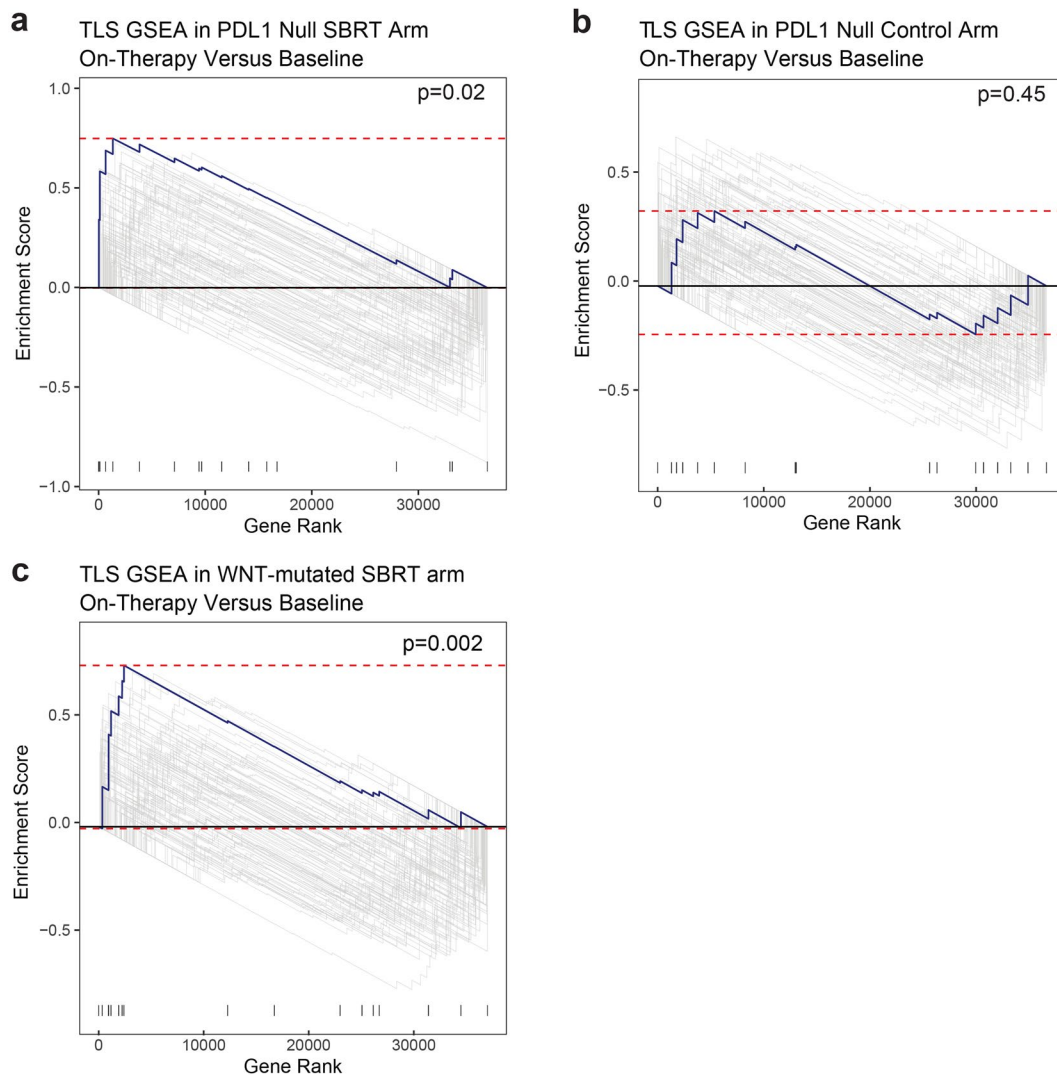
**Extended Data Fig. 5 | Tertiary Lymphoid Structure (TLS) gene set enrichment analysis from baseline to on-therapy in immunologically cold tumors.** (**a**) The TLS gene set was upregulated on-therapy in PDL-1 null tumors in the SBRT arm (GSEA (two-sided) FDR-adjusted P = 0.02). (**b**) GSEA analyses did not reveal an enrichment of the TLS gene set in PDL-1 null tumors in the control arm (GSEA (two-sided) FDR-adjusted P = 0.45). (**c**) Similarly, the TLS gene set was significantly upregulated on-therapy in WNT-mutated tumors in the SBRT arm (GSEA (two-sided) FDR-adjusted P = 0.002).

a

b
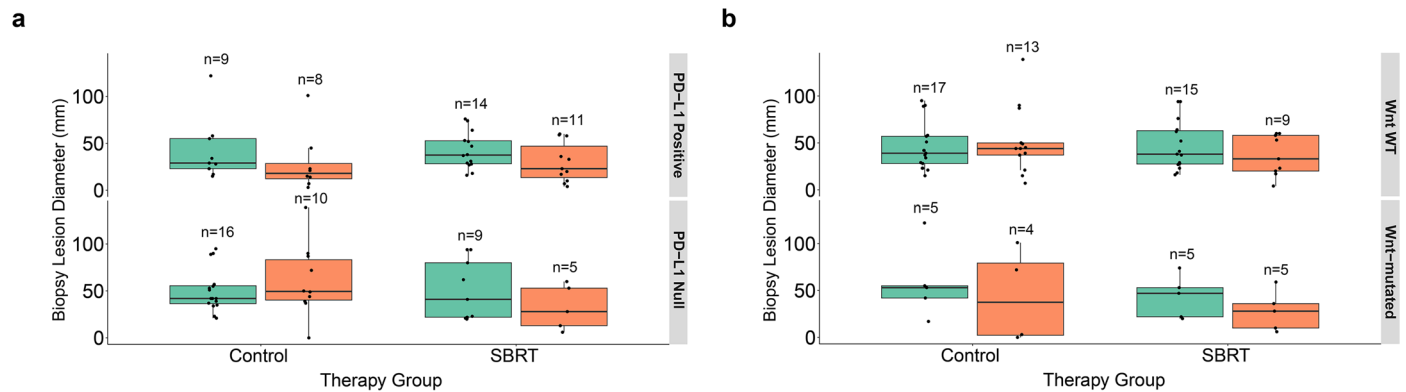
Extended Data Fig. 6 | Comparison of biopsy lesion diameter between baseline and 12 weeks on therapy. (**a**) Among PD-L1 null patients, there was a numerical reduction in biopsy lesion diameter from baseline to on-therapy in SBRT patients, but a numerical increase in diameter in control patients (PD-L1 null SBRT mean diameter at baseline 50.78 mm, mean diameter on therapy 32 mm, Mann-Whitney U test (two-sided) P = 0.29; PD-L1 null control mean diameter at baseline 50.31 mm, mean diameter on therapy 60.7 mm, Mann-Whitney U test (two-sided) P = 0.49). Numerical reductions were observed in biopsy lesion diameter between baseline and 12 weeks on therapy for PD-L1 positive patients in both treatment arms (PD-L1 positive control mean diameter at baseline 42.33, mean diameter on therapy 28.63, Mann-Whitney U test (two-sided) P = 0.11; PD-L1 positive SBRT mean diameter at baseline 42.14 mm, mean diameter on therapy 29.73 mm, Mann-Whitney U test (two-sided) P = 0.15). (**b**) Both SBRT and control patients with Wnt-mutated tumors show numerical reductions in biopsy lesion

diameters from baseline to on-therapy (Wnt-mutated SBRT mean diameter at baseline 43.2 mm, mean diameter on therapy 27.8, Mann-Whitney U test (two-sided) P = 0.42; Wnt-mutated control mean diameter at baseline 57.8 mm, mean diameter on therapy 44 mm, Mann-Whitney U test (two-sided) P = 0.73). No notable changes are observed for patients with Wnt-wild type tumors in either treatment arm (Wnt-wild type SBRT mean diameter at baseline 46.6 mm, mean diameter on therapy 36.44 mm, Mann-Whitney U test (two-sided) P = 0.36; Wnt-wild type control mean diameter at baseline 45.47, mean diameter on therapy 51.31, Mann-Whitney U test (two-sided) P = 0.72). Box plots depict the median value and hinges correspond to the first and third quartiles. The whiskers extend from the corresponding hinge to the furthest value within 1.5* the interquartile range from the hinge. Green denotes the baseline timepoint, while the on-therapy timepoint is shown in orange.
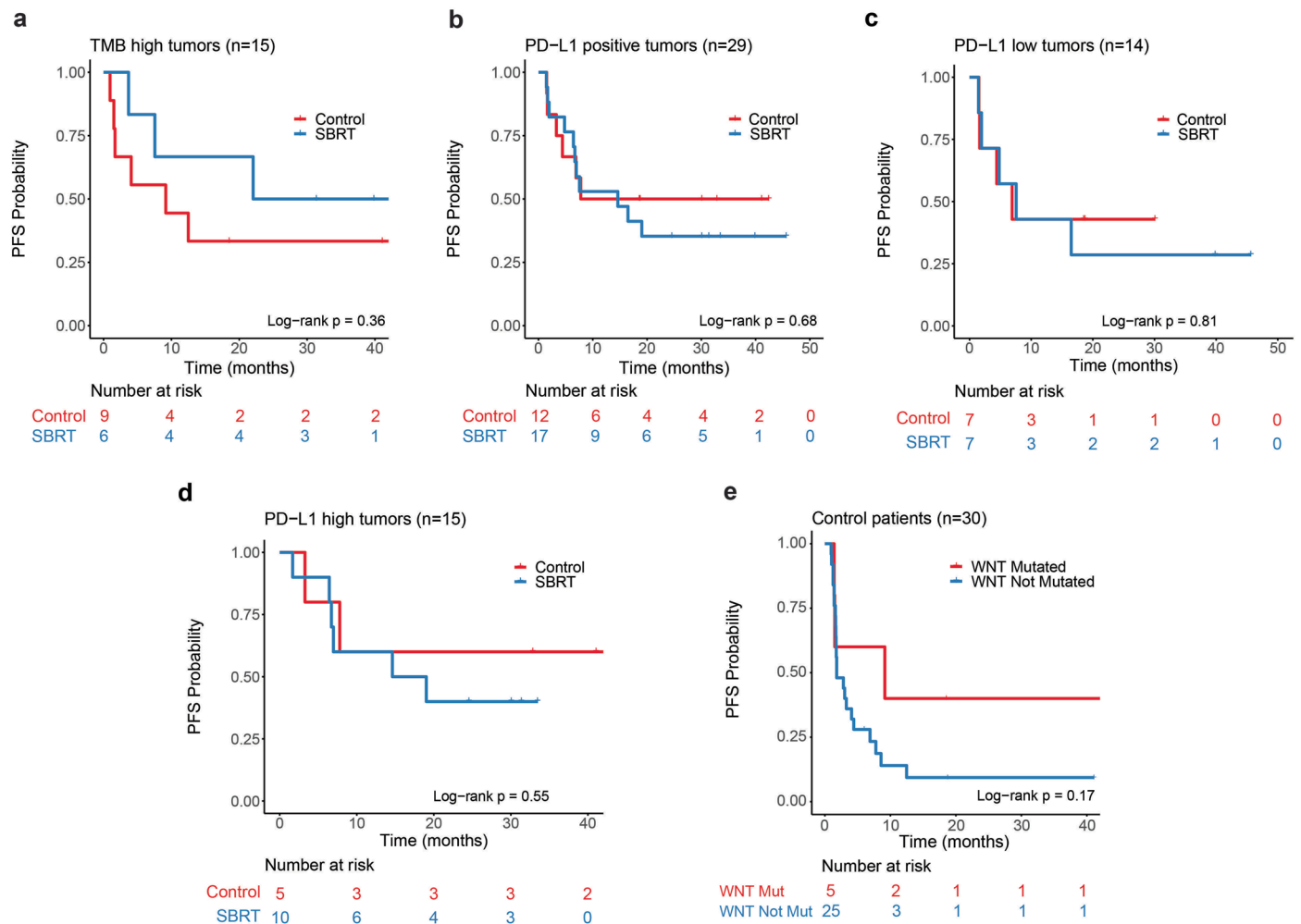
Extended Data Fig. 7 | Survival outcomes with radio-immunotherapy for patients with TMB-high, PD-L1-positive (immunohistochemistry (IHC) staining >=1%), PD-L1 low (IHC staining 1-49%) and PD-L1 high (IHC staining >=50%) tumors by treatment arm and for patients with Wnt-mutant tumors in the control arm. (**a**) Kaplan–Meier analyses for PFS in TMB-high tumors (n = 15 patients) in the control arm (n = 9 patients) and SBRT arm (n = 6 patients) did not reveal significant differences between patients in the SBRT versus control arms (median PFS 22.05 months vs 9.16 months, log-rank P = 0.36). (**b**) Kaplan–Meier analyses for PFS in PD-L1 positive tumors (n = 29 patients) in the control arm (n = 12 patients) and SBRT arm (n = 17 patients) did not demonstrate significant differences (median PFS 14.62 vs 7.79 months, log-rank P = 0.68). (**c**) Kaplan–Meier analyses for PFS in PD-L1 low tumors (n = 14 patients) in the control

arm (n = 7 patients) and SBRT arm (n = 7 patients) did not reveal significant differences between patients in the SBRT versus control arms (median PFS SBRT arm 7.56 months, control arm 6.90 months, log-rank P = 0.81). (**d**) Kaplan–Meier analyses for PFS in PD-L1 high tumors (n = 15 patients) in the control arm (n = 5 patients) and SBRT arm (n = 10 patients) did not reveal significant differences between patients in the SBRT versus control arms (median PFS SBRT arm 16.8 months, control arm median not reached, log-rank P = 0.55). (**e**) Kaplan–Meier analyses for PFS by Wnt-mutation status in the control arm (n = 30 patients) did not reveal significant differences between patients with Wnt-mutated (n = 5 patients) versus Wnt-not mutated tumors (n = 25 patients; log-rank P = 0.17). PFS: Progression Free Survival.
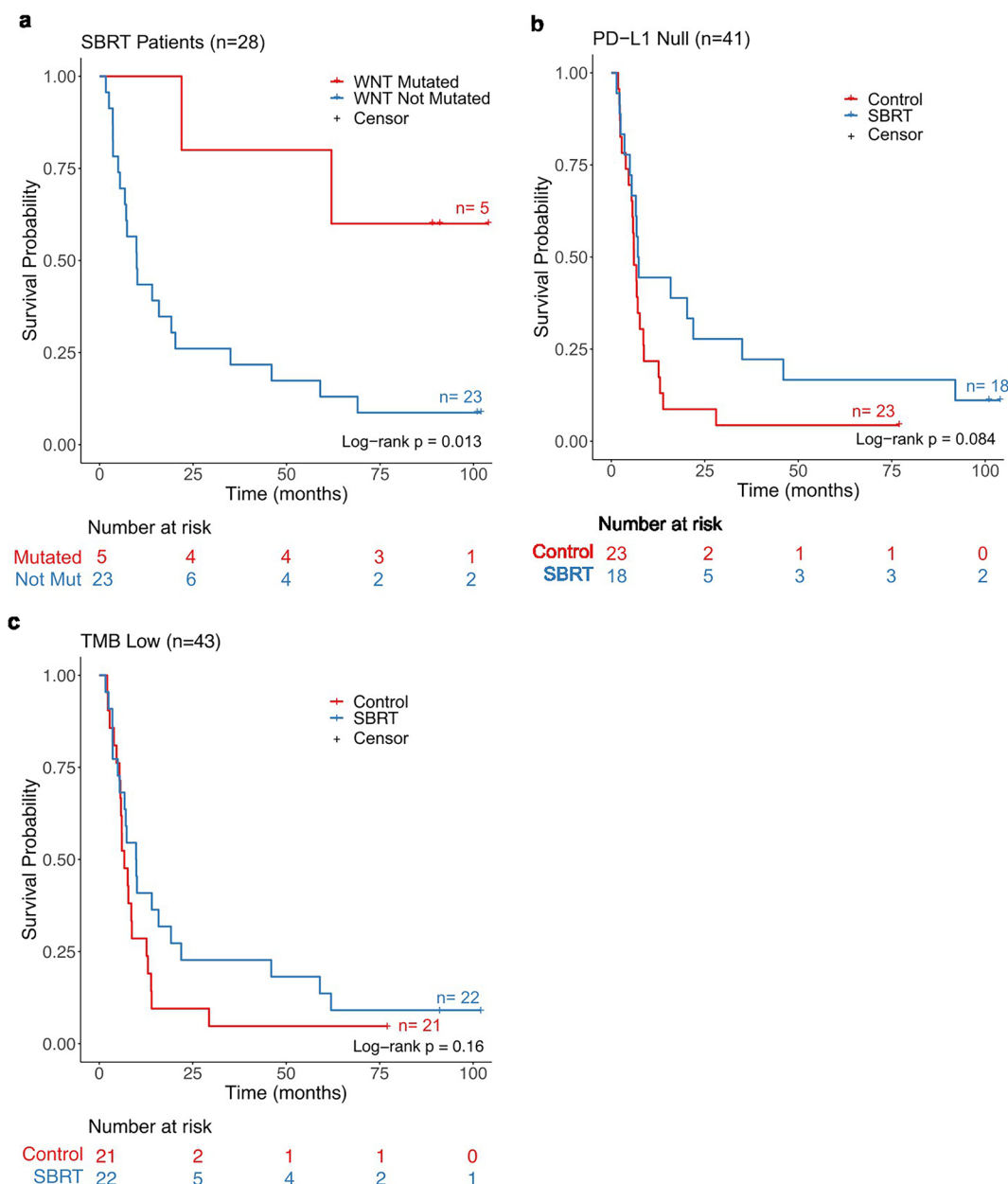
**Extended Data Fig. 8 | Overall survival outcomes for patients with tumors that are TMB-low, PD-L1-null, or harboring mutations in the Wnt pathway.** (**a**) Kaplan–Meier curve of probability of OS in PD-L1 null patients (n = 41 patients) treated in the control arm (n = 23 patients) and SBRT arm (n = 18 patients). PD-L1 null patients have a trend of longer OS in the SBRT arm than in the control arm (median OS SBRT arm 7.21 months, control arm 6.05 months, log-rank P = 0.084). (**b**) Kaplan–Meier curve of probability of OS in TMB low patients (n = 43 patients) treated in the control arm (n = 21 patients) and SBRT arm (n = 22 patients).

TMB low patients have numerically longer OS in the SBRT arm than patients in the control arm, though the difference is statistically insignificant (median OS SBRT arm 9.89 months, control arm 6.70 months, log-rank P = 0.16) (**c**) Kaplan–Meier curve of probability of OS in the SBRT arm in Wnt Mutated patients (n = 5 patients) and non-Wnt Mutated patients (n = 23 patients). Among patients in the SBRT arm, Wnt-mutated patients have longer OS than non-Wnt mutated patients (median OS Wnt mutated not reached, Wnt-wild type 9.92 months, log-rank P = 0.013). OS: overall survival.
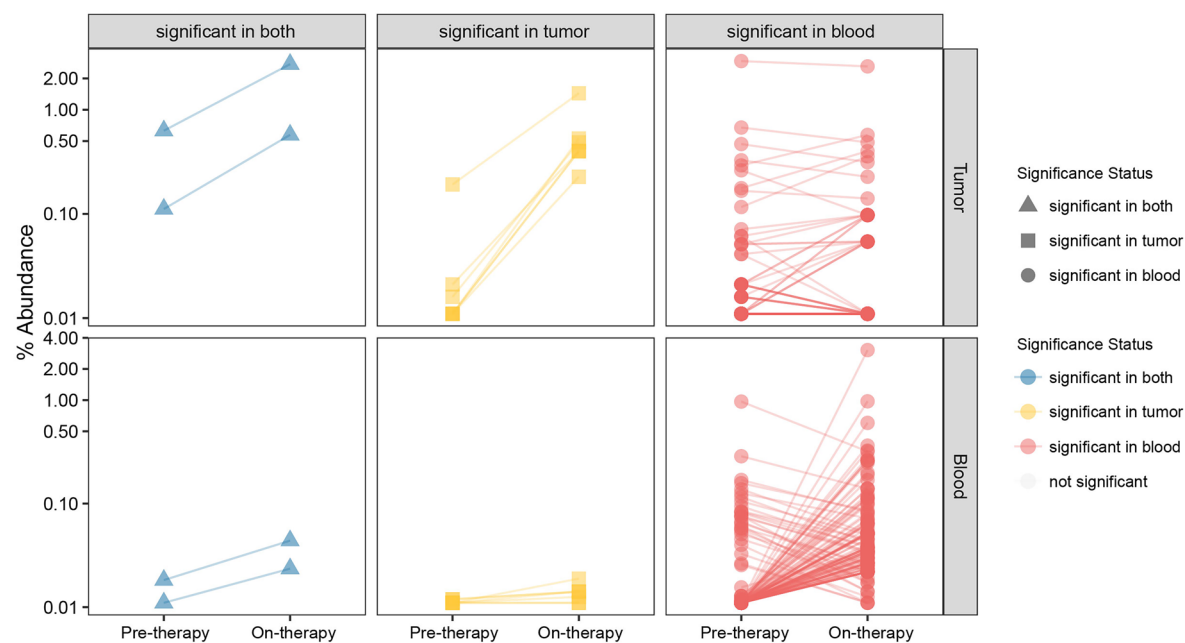
Extended Data Fig. 9 | Expansion dynamics of TCR clones that significantly expanded from baseline to on therapy in a partial responder in the SBRT cohort harboring a tumor with low TMB and null PD-L1 expression. Patient 727 had 6 new clones with significant baseline-to-on-therapy expansion in tumor, 19 new clones expanded in blood, and 2 new clones expanded in both compartments. This patient's TMB and PD-L1 statuses suggest they likely would not respond to ICI monotherapy. Thus, patient 727, who achieved partial response in the SBRT cohort, may represent a group of patients who could benefit most from SBRT-pembrolizumab dual therapy.
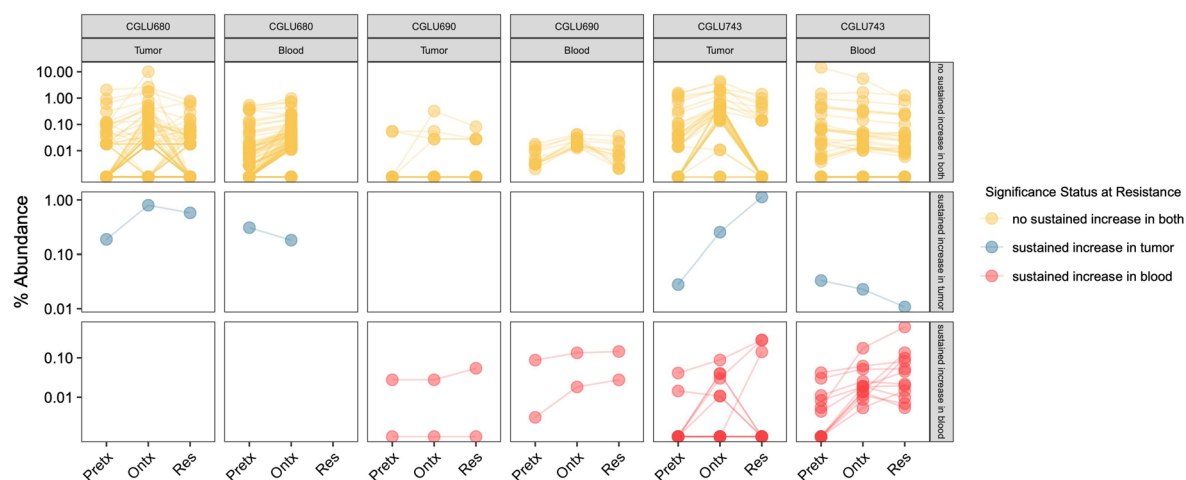
Extended Data Fig. 10 | Expansion dynamics of TCR clones from baseline to on-therapy to time of resistance in 2 partial responders in the SBRT arm and 1 partial responder in the control arm who developed resistance to treatment. Patients 680 and 690 were in the SBRT cohort, while patient 743 was in the control arm. All clones that significantly expanded from baseline to on therapy samples are visualized, stratified by location of on-therapy expansion (tumor vs blood, columns), then by expansion status at time of resistance relative to baseline abundances (no sustained increase vs sustained increase in tumor vs

sustained increase in blood, rows). Most clones that expanded on treatment in SBRT patients showed no sustained expansion at time of acquired resistance (7% sustained intra-tumoral TCR expansion, 14% sustained blood TCR expansion). Similar patterns were noted for the patient in the control arm regarding intra-tumoral TCR clones, though notably more clones remained expanded in the blood compartment at time of resistance (3% sustained intra-tumoral TCR expansion, 63% sustained blood TCR expansion).

nature portfolio

Corresponding author(s):   Valsamo Anagnostou

Last updated by author(s):   Jun 10, 2025

Reporting Summary

Nature Portfolio wishes to improve the reproducibility of the work that we publish. This form provides structure for consistency and transparency in reporting. For further information on Nature Portfolio policies, see our Editorial Policies and the Editorial Policy Checklist.

Statistics

For all statistical analyses, confirm that the following items are present in the figure legend, table legend, main text, or Methods section.

n/a	Confirmed	
☐	☒	The exact sample size (*n*) for each experimental group/condition, given as a discrete number and unit of measurement
☐	☒	A statement on whether measurements were taken from distinct samples or whether the same sample was measured repeatedly
☐	☒	The statistical test(s) used AND whether they are one- or two-sided *Only common tests should be described solely by name; describe more complex techniques in the Methods section.*
☐	☒	A description of all covariates tested
☐	☒	A description of any assumptions or corrections, such as tests of normality and adjustment for multiple comparisons
☐	☒	A full description of the statistical parameters including central tendency (e.g. means) or other basic estimates (e.g. regression coefficient) AND variation (e.g. standard deviation) or associated estimates of uncertainty (e.g. confidence intervals)
☐	☒	For null hypothesis testing, the test statistic (e.g. *F*, *t*, *r*) with confidence intervals, effect sizes, degrees of freedom and *P* value noted *Give P values as exact values whenever suitable.*
☒	☐	For Bayesian analysis, information on the choice of priors and Markov chain Monte Carlo settings
☒	☐	For hierarchical and complex designs, identification of the appropriate level for tests and full reporting of outcomes
☒	☐	Estimates of effect sizes (e.g. Cohen's *d*, Pearson's *r*), indicating how they were calculated

Our web collection on statistics for biologists contains articles on many of the points above.

Software and code

Policy information about availability of computer code

Data collection	Clinical data were collected, entered and managed according to standard data management procedures. No software was used for data collection.
Data analysis	R versions 3.6 or higher were used for statistical analyses. VariantDx was used for somatic mutation calling from whole exome sequencing data. Mutation signatures were based on the fraction of coding point mutations in each of 96 trinucleotide contexts and estimated the contribution of each signature to each tumor sample using the deconstructSigs R package (v1.8.0) with the default 'signatures.nature2013' settings. FACETS 0.6.1 was utilized for assessing the purity of individual tumor samples, generating integer allele-specific copy number profiles across the entire genome, and determining the cellular fraction associated with each aberrant somatic copy number alterations. ASCETS was used to determine the ASCETS aneuploidy score for each sample. CIBERSORT v1.06 was used to perform deconvolution of transcriptome data to determine immune cell fractions. TRUST4 was used to perform deconvolution of transcriptome data to determine B cell receptor counts. RNA-seq data were aligned to the human transcriptome using STAR-2.7.3a, followed by RSEM-1.2.30 for isoform and gene-level quantification. Normalization of raw transcript counts and differential expression analysis was performed with DESeq2 1.42.0. Normalized gene expression counts were analyzed with the fgsea48 (v.1.20.0) R package.

For manuscripts utilizing custom algorithms or software that are central to the research but not yet described in published literature, software must be made available to editors and reviewers. We strongly encourage code deposition in a community repository (e.g. GitHub). See the Nature Portfolio guidelines for submitting code & software for further information.

Data

Whole exome sequencing and RNA sequencing data are deposited and can be retrieved from the European Genome-Phenome Archive (EGA study accession EGAS50000000277, EGA dataset accession EGAD50000000404). The following Data Use Ontologies (DUO) are linked with the EGA dataset EGAD50000000404, related to privacy restrictions included in the informed consent: NPUNCU: not for profit, non commercial use only. This data use modifier indicates that use of the data is limited to not-for-profit organizations and not-for-profit use, non-commercial use; IRB: ethics approval required. This data use modifier indicates that the requestor must provide documentation of local IRB/ERB approval; US: user specific restriction. This data use modifier indicates that use is limited to use by approved users; PS: project specific restriction. This data use modifier indicates that use is limited to use within an approved project. Requests for access to the sequence data can be submitted in the EGA portal using the access codes above, after which the requestor will receive a data access agreement that needs to be filled in with respect to description of the research in which the dataset will be utilized for. Commercial/for-profit use of the dataset is not allowed per regulatory mandates and the requestor must provide documentation of local IRB approval. Following review and sign off by the requestor and the requestor's institution regulatory official, the data access agreement will be reviewed by the Office of Research Administration at the Johns Hopkins University. Following review, the agreement will be signed and sent back to the requestor. Following completion of the process above, the dataset will be released to the requestor in EGA. The timeline for the above process depends on the speed of regulatory review required. Clinical data is available upon request from Dr. Willemijn Theelen at the Netherlands Cancer Institute (w.theelen@nki.nl). Source data for all figures are provided as source data files.

Research involving human participants, their data, or biological material

Policy information about studies with human participants or human data. See also policy information about sex, gender (identity/presentation), and sexual orientation and race, ethnicity and racism.

Reporting on sex and gender	Findings apply to both sexes. Sex was determined by self-reporting, both females and males were enrolled in the study and sex was not a stratification criterion for this study.
Reporting on race, ethnicity, or other socially relevant groupings	Findings apply to all race and ethnicity groups, as race, ethnicity or other socially relevant grouping was not an inclusion or exclusion criterion in this study.
Population characteristics	We analyzed 293 serial tumor and peripheral blood samples collected at baseline and after 2 cycles of pembrolizumab from 72 patients in the control (n=37, mean age 61.8) and SBRT (n=35, mean age 61.0) arms from the previously reported PEMBRO-RT trial (NCT02492568). The previously published PEMBRO-RT trial enrolled 92 patients with advanced non–small cell lung cancer (NSCLC) between July 1, 2015 and March 31, 2018, regardless of PD-L1 status. Of those 92 patients, 76 were randomized to the control arm (pembrolizumab monotherapy, n=40) or the SBRT arm (SBRT followed by pembrolizumab, n=36). Of the 76 patients, 72 patients received at least one course of pembrolizumab and were thus included in this study.
Recruitment	Patient recruitment for the PEMBRO-RT trial has been previously published and is explicitly described in the clinical trial publication (Theelen et al., JAMA Oncol, 2019). Briefly, patients included in this study received at least one course of pembrolizumab. Patients 18 years or older were eligible to participate if they had histological or cytological confirmed metastatic non–small cell lung cancer (NSCLC) that progressed after at least 1 regimen of chemotherapy but who were immunotherapy naive and had an Eastern Cooperative Oncology Group performance status of 1 or lower. At least 2 separate lesions were required, one of which was measurable according to the Response Evaluation Criteria in Solid Tumors and suitable for biopsy, and the other of which was amenable to irradiation. Patients were ineligible if they had (1) radiotherapy to any tumor site within 6 months before randomization; (2) known, active central nervous system metastases and/or carcinomatous meningitis; (3) untreated driver alterations of epidermal growth factor receptor or anaplastic lymphoma kinase; or (4) active autoimmune or interstitial lung disease.
Ethics oversight	The study protocol and all amendments were approved by the Institutional Review Board of Johns Hopkins University (Johns Hopkins Medicine Institutional Review Board) and the Netherlands Cancer Institute Antoni van Leeuwenhoek Institutional Review Board (registered under number CFMPB573). Written informed consent was provided by all study participants; participants were not compensated.

Note that full information on the approval of the study protocol must also be provided in the manuscript.

Field-specific reporting

Please select the one below that is the best fit for your research. If you are not sure, read the appropriate sections before making your selection.

☒ Life sciences ☐ Behavioural & social sciences ☐ Ecological, evolutionary & environmental sciences

For a reference copy of the document with all sections, see nature.com/documents/nr-reporting-summary-flat.pdf

Life sciences study design

All studies must disclose on these points even when the disclosure is negative.

Sample size	As the analyses presented represent exploratory analyses, there was no formal calculation of sample size. Sample sizes were chosen based on patient enrollment in the PEMBRO-RT trial as described in Theelen et al., JAMA Oncology, 2019. No statistical methods were used to pre-determine sample sizes but our sample sizes are similar to those reported in previous publications (Anagnostou et al., Nature Cancer 2020).
Data exclusions	All patients with available data were included.
Replication	The analytical performance of the multi-omics assays used in this study has been previously extensively validated, as referenced in the methods section of the manuscript. For functional T cell analyses via the MANAFEST assays, technical replicates were performed. For patients CGLU690 and CGLU727, for whom adequate numbers of PBMCs were available for triplicate analyses, we analyzed TCR clone abundances per subject timepoints across peptide stimulation configurations. Multiple replicates per configuration were evaluated by (1) determining the set of TCR clones that were positive in the majority of replicates available for a given configuration, and (2) determine which were at least 5x fold change (FC) greater in percentage abundance in the target condition (as measured by the lowest positive value) than the next highest single replicate from a different configuration.
Randomization	This is not applicable for the exploratory multi-omic analyses reported in this study. In the original PEMBRO-RT study (Theelen et al., JAMA Oncology), patients were randomly assigned using a 1:1 ratio to receive treatment with pembrolizumab either after SBRT to a single tumor site (experimental arm) or without SBRT (control arm) as part of the PEMBRO-RT trial and samples from these patients were leveraged in this study.
Blinding	While blinding is not entirely relevant outside the context of a clinical trial, clinical data collection and clinical trial endpoint determination was performed independent of the conditions of the experiments.

Reporting for specific materials, systems and methods

We require information from authors about some types of materials, experimental systems and methods used in many studies. Here, indicate whether each material, system or method listed is relevant to your study. If you are not sure if a list item applies to your research, read the appropriate section before selecting a response.

Materials & experimental systems

n/a	Involved in the study
☐	☒ Antibodies
☒	☐ Eukaryotic cell lines
☒	☐ Palaeontology and archaeology
☒	☐ Animals and other organisms
☐	☒ Clinical data
☒	☐ Dual use research of concern
☒	☐ Plants

Methods

n/a	Involved in the study
☒	☐ ChIP-seq
☒	☐ Flow cytometry
☒	☐ MRI-based neuroimaging

Antibodies

Antibodies used	PD-L1 expression was assessed after the study was closed at the Netherlands Cancer Institute by the PD-L1 IHC 22C3 LDT assay (Agilent) in formalin-fixed tumor samples from tumor tissue received at baseline.
Validation	As per the manufacturer's website, the assay used above is extensively validated.

Clinical data

Policy information about clinical studies

All manuscripts should comply with the ICMJE guidelines for publication of clinical research and a completed CONSORT checklist must be included with all submissions.

Clinical trial registration	ClinicalTrials.gov identifier NCT02492568.
Study protocol	The full trial protocol has been previously published (see Theelen WSME, Peulen HMU, Lalezari F, et al. Effect of Pembrolizumab After Stereotactic Body Radiotherapy vs Pembrolizumab Alone on Tumor Response in Patients With Advanced Non–Small Cell Lung Cancer: Results of the PEMBRO-RT Phase 2 Randomized Clinical Trial. JAMA Oncol. 2019;5(9):1276–1282. doi:10.1001/jamaoncol.2019.1478).
Data collection	For the clinical trial and as previously published, between July 1, 2015, and March 31, 2018, 92 patients with advanced non–small cell lung cancer (NSCLC) were screened for enrollment at the NKI-AVL, and 76 patients who met the eligibility criteria were randomly assigned to either the control arm (n=40) or the experimental arm (n=36). Of the 76 patients, 72 patients received at least one

course of pembrolizumab and were thus included in this study.

| Outcomes | Clinical endpoints for the PEMBRO-RT trial are described in the original publication (Theelen et al., JAMA Oncol, 2019). |

Plants

| Seed stocks | Not applicable. |

| Novel plant genotypes | Not applicable. |

| Authentication | Not applicable. |